The Evolution of Field Early–Type Galaxies in the FDF and WHDF†

Alexander Fritz,[1,2,3]⋆ Asmus Böhm,[4] and Bodo L. Ziegler[5]

[1]*Gemini Observatory, 670 N. A'ohoku Place, Hilo, HI 96720, USA*
[2]*Department of Physics and Astronomy, University of Pennsylvania, 209 South 33rd Street, Philadelphia, PA 19104-6396, USA*
[3]*Institut für Astrophysik Göttingen, Friedrich-Hund-Platz 1, 37077 Göttingen, Germany*
[4]*Astrophysikalisches Institut Potsdam, An der Sternwarte 16, 14482 Potsdam, Germany*
[5]*European Southern Observatory, Karl-Schwarzschild-Strasse 2, 85748 Garching bei München, Germany*

15 June 2013

ABSTRACT

We explore the properties of 24 field early–type galaxies in the redshift range $0.20 < z < 0.75$ down to $M_B \leq -19.30$ in a sample extracted from the FORS Deep Field and the William Herschel Deep Field. Target galaxies were selected on the basis of a combination of luminosity, spectrophotometric type, morphology and photometric redshift or broad–band colours. High signal–to–noise intermediate–resolution spectroscopy has been acquired at the Very Large Telescope, complemented by deep high-resolution imaging with the Advanced Camera for Surveys onboard the *HST* and additional ground–based multi–band photometry. All galaxy spectra were observed under sub–arcsecond conditions and allow to derive accurate kinematics and stellar population properties of the galaxies. To clarify the low level of star formation detected in some galaxies, we identify the amount of active galactic nuclei (AGN) activity in our sample using archive data of *Chandra* and *XMM-Newton* X-ray surveys. Non of the galaxies in our sample were identified as secure AGN source based on their X-ray emission. The rest-frame B and K-band scaling relations of the Faber-Jackson relation and the Fundamental Plane display a moderate evolution for the field early–type galaxies. Lenticular (S0) galaxies feature on average a stronger luminosity evolution and bluer rest-frame colours which can be explained that they comprise more diverse stellar populations compared to elliptical galaxies. The evolution of the FP can be interpreted as an average change in the dynamical (effective) mass-to-light ratio of our galaxies as $\langle \Delta \log (M/L_B)/z \rangle = -0.74 \pm 0.08$. The M/L evolution of these field galaxies suggests a continuous mass assembly of field early-type galaxies during the last 5 Gyr, that gets support by recent studies of field galaxies up to $z \sim 1$. Independent evidence for recent star formation activity is provided by spectroscopic ([O II] emission, Hδ) and photometric (rest–frame broad–band colors) diagnostics. Based on the Hδ absorption feature we detect a weak residual star formation for galaxies that accounts for 5%–10% in the total stellar mass of these galaxies. The co-evolution in the luminosity *and* mass of our galaxies favours a downsizing formation process. We find some evidence that our galaxies experienced a period of star formation quenching, possible triggered by AGN activity that is in good agreement with recent results on both observational and theoretical side.

Key words: cosmology: observations – galaxies: elliptical and lenticular, cD – galaxies: evolution – galaxies: formation – galaxies: kinematics and dynamics – galaxies: stellar content

1 INTRODUCTION

Early–type galaxies (the family consisting of elliptical and lenticular galaxies, hereafter E+S0 galaxies) represent one of the most important diagnostics within the cosmological picture of galaxy formation and evolution. E+S0 galaxies and bulges comprise most of the baryonic (stellar) mass (50% or more of all stellar spectral types) in the present-day universe (e.g., Bell et al. 2003) and reside in the most massive dark matter haloes with halo masses up to $M_{\rm h} \sim 4 \times 10^{13} h^{-1} M_\odot$ at $z = 0$, hence these systems are the key ingredients for understanding the star formation and the mass assembly history of the galaxy population as a whole and for the

structure formation starting from the early primordial stages of the universe.

Early hierarchical structure formation models based on Cold Dark Matter particles predict different evolutionary paths and assembly time–scales for the densest environments of clusters of galaxies and the lowest densities of isolated galaxies (e.g., Kauffmann 1996; Baugh et al. 1998; Somerville & Primack 1999; Cole et al. 2000). From typical age variations of 43% in the overall stellar content between cluster and field galaxies, a late mass assembly for massive E+S0 galaxies of smaller sub–units is expected with the involved physical processes (mainly star formation rates, gas cooling and heating) poorly understood. As a consequence, the simplified baryonic recipes are interpreted and implemented differently in the simulations (Benson et al. 2002). In this paradigm, field early–type galaxies are assembled through merging and accretion events of smaller clumps and fragments on longer time–scales up to the recent past (Diaferio et al. 2001; De Lucia et al. 2004). The environment is therefore suggested to play an important role to constrain the formation and evolution of E+S0 galaxies and their internal properties. These predictions have significant imprints for the abundance and mass distribution of an existing or even fully established population of old massive systems at $1 \leq z \leq 2$ (Glazebrook et al. 2004; Bundy et al. 2006; Cimatti et al. 2006; Borch et al. 2006; Conselice et al. 2007) and also for recent claims of the detection of their possible progenitors at high redshifts of $z > 2$ (Chapman et al. 2004; Kriek et al. 2006; Cimatti et al. 2006; McGrath et al. 2007).

Over the past few years theoretical semi-analytic models of galaxy formation have been improved dramatically. By including a secondary star burst mode to the previous quiescent star formation history, i.e. allowing a fraction of gas to be directly transformed into stars in merging galaxies (Kauffmann & Haehnelt 2000; Somerville et al. 2001), an increasing amount of supernova feedback and/or an additional effect of Active Galactic Nuclei (AGN) feedback (Granato et al. 2004; Croton et al. 2006; Bower et al. 2006; De Lucia et al. 2006) or virial shocks of infalling gas in a spherical halo (Birnboim et al. 2007) to suppress the remaining star formation activity, a much better agreement with the observations has been achieved. The suppression of star formation in massive halos using primarily AGN feedback has a strong impact at the top of the luminosity function (LF) that results in a far less overproduction of massive galaxies at $z = 0$ than earlier simulations, while still providing a good description of the rest of the observed LF up to $z \simeq 1.5$ (Bower et al. 2006). However, there is still a non-negligible excess of local luminous galaxies detectable in the local simulated LF, which models adjust by including additional internal dust obscuration or a relative inefficiency of the stellar mass of merging galaxies that results in a population of free-floating intergalactic stars (Monaco et al. 2006).

Previous studies have quantified to detect the deviations from passive evolutionary tracks as predicted by semi-analytic models in the evolution of the Fundamental Plane (FP; Djorgovski & Davis 1987; Dressler et al. 1987). This relationship is constructed among the basic parameters of E+S0 galaxies, their size (the half-light effective radius R_e in kpc), stellar kinetic energy (central velocity dispersion σ in km s^{-1}) and luminosity (average surface brightness within R_e, $\langle \mu_e \rangle$, in units of mag arcsec^{-2}) and provides a powerful tool to measure the the evolution of the mass-to-light (M/L) ratio as a function of redshift without being subject to uncertainties in the photometric model estimates, such as initial mass function or age and/or metallicity degeneracy. Using this observational technique cluster early–

type galaxies formed the majority of their stars at redshifts $z \geq 2$ and their stellar populations follow a slow passive evolution since then (e.g., van Dokkum & Franx 1996; Bender et al. 1998; van Dokkum & Stanford 2003; Fritz et al. 2005; Jørgensen et al. 2006). However, the cosmic formation epoch and evolutionary history of isolated field galaxies remains unclear. Indeed, galaxy formation models based on a hierarchical structure growth envision for a given galaxy mass a dependence on environment (Diaferio et al. 2001). At a given redshift this environmental effect results in explicit age variations between E+S0 galaxies in clusters and in low–density regions, where cluster ellipticals show an average luminosity–weighted age of 9.6 Gyr, whereas field E+S0s being by ∼4 Gyr younger and displaying a broader age spread than their counterparts in clusters (Cole et al. 2000). In addition, brighter (and hence more massive) field galaxies ($M_B < -20.1$) should feature on average ∼2 Gyr younger ages than fainter ones and comprise more metal rich $0.05 \leq$ [Fe/H] ≤ 0.1 dex populations than their cluster representatives (Thomas et al. 2005), but no differences in their element abundance ratios (α/Fe).

So far, for the field galaxy population inconsistent results have been derived. Some studies suggest an evolution similar to early–type galaxies in clusters (van Dokkum et al. 2001a; Treu et al. 2001; van de Ven et al. 2003; van Dokkum & Ellis 2003; Ziegler et al. 2005), but others prefer a faster mass assembly over a shorter time period since $z \sim 1$ (Treu et al. 2002; Gebhardt et al. 2003). Recently, Treu et al. (2005) performed a comprehensive investigation of early-type field galaxies within the GOODS-N field and detected evidence for a mass dependent evolution. Similar results were derived by van der Wel et al. (2005) and di Serego Alighieri et al. (2005) from an analysis of field E+S0 galaxies in the CDFS. However, although these samples were drawn from the same field they rather found incomparable galaxy sizes and velocity dispersions for individual objects (see § 6 for more details). Moreover, the different target selection procedures among the studies (e.g., magnitude, colour, morphology) might induce some inconsistency in the final sample, for example selecting galaxies with the reddest colours would favour the more massive systems where variations are less pronounced or using low signal-to-noise (S/N) spectra limits the detection post-starburst galaxies or the contamination by bulge-dominated spiral galaxies. Furthermore, difficulties may arise from the small number statistics of some works and the impact of cosmic variance remains yet to be unknown and hard to distinguish from the used sample selection (e.g., van der Wel et al. 2005; di Serego Alighieri et al. 2005, but see § 6). There is clear evidence that the interpretations of measurements are highly sensitive to selection effects and high-quality spectroscopic data is stringent necessary to allow a careful analysis of the properties of galaxies at high redshift.

In the present work, we aim to analyse in detail the assembly history and the stellar populations of a carefully selected sample of 24 early-type field spheroidal galaxies down to $M_B \leq -19.30$ in two deep sky surveys, the FORS Deep Field and the William Herschel Deep Field, by using a combination of high signal-to-noise VLT spectroscopy together with deep ground-based multi–band imaging and high-resolution space-based photometry. Although our study is restricted to small number statistics, our data is based on high-quality spectra providing both precise kinematic and stellar population properties. In a future work, we are aiming to disentangle both difficulties of high redshift investigations related to small number statistics and cosmic variance (A. Fritz et al. 2009a, in preparation).

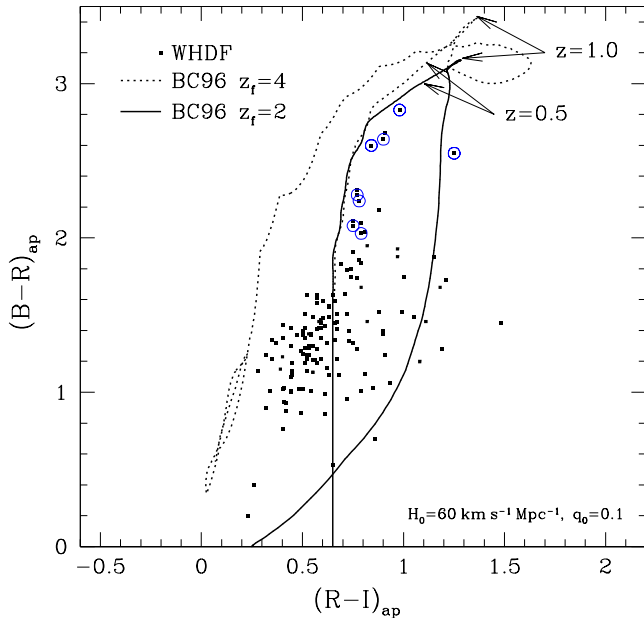The structure of this paper is as follows. In section §2, the sam-

Figure 1. $(B - R)$–$(R - I)$ colour-colour diagram for the WHDF field galaxies. Spiral candidates (squares) are displayed with the final observed field early-type galaxies (circles) and compared to evolutionary tracks for E/S0 with different formation redshifts of $z_\mathrm{f} = 2$ (solid line) and $z_\mathrm{f} = 4$ (dotted line) predicted by the burst BC96 models. For the BC96 models a cosmology with $H_0 = 60\,\mathrm{km\,s^{-1}\,Mpc^{-1}}$ and $q_0 = 0.1$ was adopted.

ple selection, observations and the kinematic analysis of the spectroscopic data are described. The photometric observations together with the derivation of structural parameters, galaxy morphologies and spectrophotometric properties are presented in section §3. Here also a discussion on available X-ray data is given. The scaling relations for field early-type galaxies are presented in §4, and the implication of these results on their formation is discussed in §5. A comparison with previous works is given in §6, followed by a discussion in §7. The main conclusions and results are summarised in §8. Throughout this article the concordance cosmology for a flat, low-density Universe is assumed with $\Omega_m = 0.3$, $\Omega_\Lambda = 0.7$ and $H_0 = 70\,\mathrm{km\,s^{-1}\,Mpc^{-1}}$. Unless otherwise noted, all magnitudes are given in the Vega-system.

2 SPECTROSCOPY

2.1 Sample Selection

Target objects were selected based upon deep $UBgRI$ and BRI multi-band imaging surveys of the FORS Deep Field (FDF, Heidt et al. 2003) and William Herschel Deep Field (WHDF, Metcalfe et al. 2001), respectively. The 50% completeness limits of the FDF and WHDF are $B = 27.7$ and $B = 27.9$, respectively. Early-type candidates were selected according to their (i) total apparent magnitude $R \leq 22.0^m$, (ii) spectrophotometric type, (iii) elongated structureless appearance and (iv) photometric redshift (only available for the FDF). The constraint in the apparent brightness ensured a sufficient signal-to-noise of $S/N \geq 15$ in the absorption lines, mandatory for a robust determination of velocity dispersions and line-strengths measurements. For this reason, faint early-type candidates with apparent magnitudes $R > 20.5^m$ were included in more than one MOS setup and the individual spectra combined after data reduction.

Spectrophotometric types and estimated redshifts were selected from the FDF photometric redshifts catalogue of more than 3800 objects (Bender et al. 2001). Only candidates with an early (E/S0) model Spectral Energy Distribution (SED) were considered and the photometric redshifts were restricted to $z_\mathrm{phot} \leq 0.6$. Based on the photometric redshifts, the elliptical candidates were spread out on different CCD positions among the spirals, which were observed for a similar project studying the Tully–Fisher relation of late–type galaxies, for each MOS setup in the observed spectral wavelength range such that either the Mg_b-feature passband ($\lambda_0 \approx 5170\,\text{Å}$) or the G-band ($\lambda_0 \approx 4300\,\text{Å}$) was included. For a reliable star/galaxy separation, targets with insignificant photometric redshift and large uncertainty (i.e., $z_\mathrm{phot} - dz_\mathrm{phot} \leq 0$) were discarded. Field candidates were selected from a deep FORS2 I-band reference image consisting of 10 seeing averaged I-band images (between 0.47–0.50 arcsec FWHM) with a final integration time of 3000 sec and a Point-Spread-Function (PSF) of 0.49 arcsec FWHM. In case of the FORS1 observations, the target selection was based on a FORS1 I-band reference image with a PSF of 0.52 arcsec FWHM. In the WHDF, field objects were drawn from a deep over five individual exposures averaged I-band reference image with a total integration time of 1500 sec and a PSF of 0.6 arcsec FWHM. To avoid misclassifications, detections of the Source Extractor package (SExtractor; Bertin & Arnouts 1996) that exhibited a star classification parameter $\texttt{star} \geq 0.9$ and $a \approx b \approx 2.5$ pixel were most likely bonafide stellar objects and were therefore rejected.

Apart from photometric redshifts, the target selection for the WHDF field early-type galaxies was performed with the same constraints as for the FDF field elliptical galaxies. Redshifts of field early-type candidates were estimated using a combination of colour-colour diagrams and apparent magnitudes. Figure 1 illustrates the target selection of the WHDF field elliptical candidates in the $(B - R)$–$(R - I)$ colour-colour diagram. The total WHDF spectroscopic data and the actually observed WHDF field ellipticals are compared to evolutionary tracks for E/S0 with different formation redshifts of $z_\mathrm{f} = 2$ (solid line) and $z_\mathrm{f} = 4$ (dotted line) as predicted by the passive evolution models for a simple (single burst) stellar population of Bruzual & Charlot [1]. Note, that the BC96 models have been computed for a slightly different cosmology with $H_0 = 60\,\mathrm{km\,s^{-1}\,Mpc^{-1}}$ and $q_0 = 0.1$. In the $(B - R)$–$(R - I)$ colour-colour diagram elliptical and spiral galaxies (Böhm & Ziegler 2007) are well separated up to $z \approx 0.5$ (indicated by the arrows) and follow the predictions of the evolutionary models quite well. To avoid a selection of high redshift elliptical galaxies with $z > 1$, the apparent R magnitude was used as an additional constraint. Although the BC96 models represent more a generalisation of the various stellar populations of early-type galaxies, together with the cut in magnitude they provide a good separation between high redshift interlopers and lower redshift galaxies which we were interested in. More complex model star formation histories (cf. Gavazzi et al. 2002) are beyond the scope of this paper. To allow a better estimate of the star formation histories of the galaxies in our sample, we will utilise absorption line indices and other spectral diagnostics in a future work (A. Fritz et al. 2009b, in

---

[1] For consistency with previous works (e.g., van Dokkum et al. 2001a), evolutionary models have been computed using the Bruzual & Charlot stellar population synthesis models (GISSEL96 version, hereafter BC96). Throughout the analysis a Salpeter (1955) initial mass function (IMF), solar metallicity and Kurucz atmosphere models are adopted.

preparation). As shown in Figure 1, galaxies populating a narrow range in the colour-colour diagram of $2 \gtrsim (B - R) \gtrsim 2.9$ and $0.7 \gtrsim (R - I) \gtrsim 1.1$ have been selected as bonafide field ellipticals and successfully verified. One object (ID 14) initially selected as an early-type candidate with $(R - I) = 0.79$, $(B - R) = 1.78$ and $R = 19.04^m$ ($z = 0.1060$) is an intermediate-type Sc spiral galaxy and was therefore discarded. It turned out that this galaxy is a spiral galaxy with a clearly visible disc on the ACS images which were not available at the time of the target selection.

2.2 Observations

Spectroscopic observations of the sample of field early-type galaxies were performed simultaneously with those of the late-type galaxies which were subject to the investigation of the evolution of the Tully–Fisher relation in the FDF (Ziegler et al. 2002; Böhm et al. 2004) and in the WHDF (Böhm & Ziegler 2007). As the target selections and instrument configurations were very similar the two individual data sets are discussed in combination.

Multi-object spectroscopy (MOS) was conducted at the Very Large Telescope (VLT) using the FOcal Reducer and low dispersion Spectrograph 2 (FORS2; Appenzeller et al. 1998) instrument in September and October 2000, July and October 2002 and FORS1 in December 1999 and October 2001. During these observations, a total of 220 galaxy spectra have been acquired under mostly excellent seeing conditions. Using the grism 600R with the order separation filter GG435+81 and slit width of 1.0 arcsec resulted in spectral resolutions of $R \approx 1200$ for the FDF observations. For the WHDF run, the volume phased holographic grism 600RI was chosen, which is even more efficient at redder wavelengths (>8000Å) than the grism 600R and has a resolution of $R \approx 1000$. Both versions of FORS instruments offer 19 slitlets in the MOS configuration, 9 with slit lengths of 22 arcsec, 8 with slit lengths of 20 arcsec, whereas the uppermost and lowermost slits have lengths of ~ 11 arcsec. The total integration time for each setup was 2.5 hours. Seeing conditions ranged between 0.43 arcsec and 0.92 arcsec FWHM, with a median of 0.76 arcsec. In order to limit the corrections of atmospheric absorption, the airmass was constraint to $A \leq 2.0$. FORS was operated at standard resolution setup, i.e. CCD read out in one-port mode. In low gain mode (using port A) FORS1 offers a gain of $3.51\,e^-$/ADU and a read-out-noise (RON) of RON=$7.21\,e^-$, resulting in a spatial scale of 0.2 arcsec/pixel for the FDF spectra. After the FORS2 detector system upgrade which was available for science use in March 2002, the standard setup offers a gain of $0.70\,e^-$/ADU and RON of $2.7\,e^-$. The spatial sampling in the final WHDF spectra was 0.25 arcsec/pixel. More details on the observations can be found in Ziegler et al. (2005) and Fritz (2006). Table 1 summarises the spectroscopic observations of the field early-type candidates in the FDF. Columns give the date of the observation, the mean airmass and mean Differential Image Motion Monitor (DIMM) seeing value during the observations, the number of E/S0 galaxies and anonymous galaxies (additional fill–up objects with no z_{phot}) for each MOS setup. Galaxies which were observed twice are counted only once in the total number of objects. A total of nine MOS setups yielded a final sample of 39 E+S0 galaxies, regardless of their environment (see further discussion in § 2.3.3). Table 2 gives an outline of the observations for the field early-type galaxies in the WHDF. In total, six different MOS setups with various MOS mask orientations depending on the interested position angles of the spiral galaxies were observed, in order to fulfill both requirements for spirals, disc inclination angles of $i > 40°$ and restricted misalign-

Table 1. VLT observations of early-type galaxies in the FDF. Repeat observations are considered only once in the total number of objects.

Tel./Instrument	Date (m/d/y)	airm.	DIMM	E+S0	anon.
VLT/FORS2	09/27/00	1.21	0.51″	5	1
	09/27/00	1.33	0.43″	5	-
	10/04/00	1.40	0.81″	6	1
	10/05/00	1.36	0.80″	5	2
	10/05/00	1.28	0.74″	8	-
	10/06/00	1.15	0.66″	7	2
	$\sum$			28	6
VLT/FORS1	12/00/99	1.08	0.66″	1	0
	10/12/01	1.43	0.76″	6	1
	10/14/01	1.07	0.89″	5	0
	10/12/01	1.38	0.82″	5	3
	$\sum$			11	4

Table 2. VLT/FORS2 observations of early-type galaxies in the WHDF. Repeat observations are considered only once in the total number of objects.

MOS	Date (m/d/y)	airm.	DIMM	E+S0	anon.
1	07/10, 10/03/02	1.18	0.64″	1	1
2	08/07, 09/11/02	1.19	0.73″	2	-
3	08/04, 08/07/02	1.51	0.92″	3	-
4	08/04, 10/02/02	1.13	0.89″	3	1
5	09/10, 09/12/02	1.18	0.91″	2	-
6	09/12, 10/4-5/02	1.14	0.85″	2	-
	$\sum$			11	1

ment angles of $\delta < 15°$ between apparent major axis and slit orientation (cf. Böhm & Ziegler 2007). Each setup was splitted into three single exposures of 3000 sec with a total integration time of 2.5 hours. and typically comprised 2–3 early-type candidates. Two additional objects (one in setup 4 and one in setup 1) fell by coincidence into a slit of a target galaxy. One object (ID 810b) turned out to be a field S0 galaxy at $z = 0.2118$. The other object is a background spiral galaxy at $z = 0.5569$ and thus was discarded. Therefore, the total sample of WHDF elliptical galaxies comprises eleven field early-type galaxies.

2.3 Spectroscopic Analysis

2.3.1 Data Reduction

Image reduction followed the standard procedure of overscan subtraction, flat–fielding, sky background subtraction, and wavelength calibration as described in Fritz et al. (2005) and Fritz (2006). Because spectra particularly near to the edges of the MOS frame exhibited spatial distortions, images of each individual slitlet were extracted from the full frame after bias subtraction allowing the typical two-dimensional image reduction of long-slit spectroscopy. The night sky background was subtracted by iteratively fitting each CCD column separately using a polynomial fit of first or zero order. During the wavelength calibration, for the dispersion relation typical rms values of 0.04 Å at a dispersion of ~ 1.62 Å/pixel were achieved. After the wavelength calibration, spectra of the respective
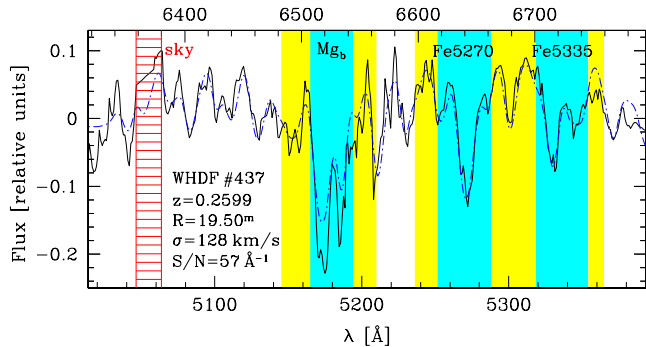
Figure 2. Example of a velocity dispersion measurement for a typical S/N spectrum of a field galaxy in the WHDF. The galaxy spectrum (solid line) is compared to the stellar template (blue dot-dashed line) that was smeared to the σ of the galaxy. Absorption lines of Mg_b, Fe 5270 and Fe 5335 are shown, splitted into their defined feature passbands (blue and red continuum and central passband), indicated as shaded regions. The hatched spectral region is affected by the telluric line at $\lambda = 6367$ Å and was masked out during the fit. The upper (lower) abscissa displays the spectrum in observed (rest-frame) wavelength units, the inset shows the derived quantities.

Figure 3. Redshift distribution of the early–type galaxies within the FDF and WHDF. The median redshift of the total field early–type galaxy sample is $\langle z \rangle = 0.40$ and is indicated with an arrow. Early–type galaxies within the FDF that were spectroscopically confirmed to be members of a cluster at $z \approx 0.34$ are also shown. Note that these cluster galaxies are not entering our field sample.

exposures were summed up and the spectral rows corresponding to the full-width at half maximum (FWHM) of an object were averaged along the dispersion direction using a Horne-based algorithm (Horne 1986). We also compared this method to a different slit extraction technique using equal-weight extractions which yielded to the same velocity dispersion measurements within their uncertainties (Fritz 2006). In those cases where a galaxy was observed in two different MOS setups, the wavelength ranges covered did not match each other exactly leading to varying final count rates at different wavelengths.

2.3.2 Velocity Dispersions

Internal velocity dispersions (σ) and radial velocities ($v_{\rm rad}$) of the galaxies were computed using an updated version of the *Fourier Correlation Quotient* (FCQ) method (Bender 1990), as described in Fritz et al. (2005) and Ziegler et al. (2005). A brief summary follows. The algorithm is based on the deconvolution of the peak of the template-galaxy correlation function with the peak of the autocorrelation function of a template star. In comparison to other procedures (Sargent et al. 1977; Tonry & Davis 1979), the main advantages of the FCQ method are the possibility to *a posteriori* chose the most appropriate function to approximate the Line-Of-Sight-Velocity-Distribution (LOSVD), a very high robustness against template mismatch and a high insensitivity due to metallicity differences in the spectra. For sufficient high S/N spectra of 10 per pixel, even velocity dispersions of $0.5 \times \sigma_i$, with σ_i being the instrumental resolution, can be determined with a high degree of accuracy. For each galaxy, σ and $v_{\rm rad}$ were measured around the spectral wavelength range of the G4300-band (hereafter G-band), the Mg_b and the $H\beta$ feature in Fourier space by convolving a template spectrum with a Gaussian to match the width of absorption lines in the observed galaxy spectrum of interest. Spectral regions that suffered from strong night sky emission lines, sky subtraction residuals defects or the A- or B-band absorption caused from the terrestrial atmosphere were carefully masked out during the fitting process. In 10 out of 24 cases, at least two different wavelength regimes could be analysed. For all early-type galaxy candidates the signal-to-noise in the spectra was sufficient to yield very sta-
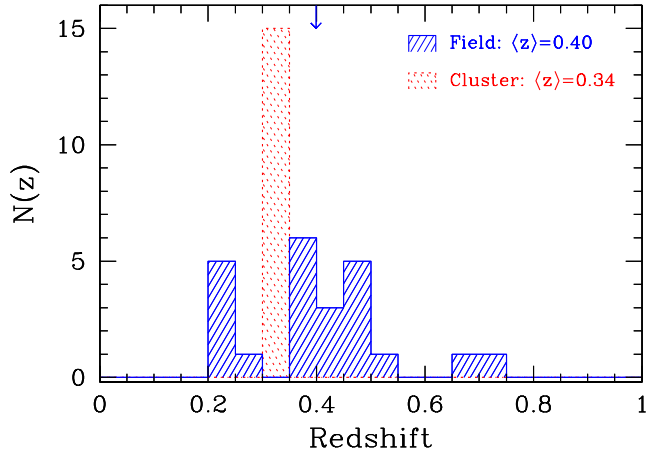
ble stellar velocity dispersion measurements (see Appendix § A for a discussion). Deviations in σ from template to template are small and ranged from 2 to $20 \, {\rm km \, s^{-1}}$. Since only one good template star (SAO 162947) was available that was observed under the same FORS instrumental configurations as the galaxies, three more K giant stars (SAO 32042, SAO 80333 & SAO 98087) were used which had been observed with MOSCA at the 3.5m-telescope at the Calar Alto observatory (Fritz 2006, A. Fritz et al. 2009c, in preparation). These templates have sufficiently resolved spectra with instrumental resolution of $\sigma_* \approx 55 \, {\rm km \, s^{-1}}$ around Mg_b and $\sigma_* \approx 69 \, {\rm km \, s^{-1}}$ around the G-band.

To determine the instrumental resolution of the galaxy spectra, the widths of 12–14 unblended and not-saturated HgAr/Ne emission lines of the respective wavelength calibration frames were measured at wavelengths corresponding to Mg_b and the G-band separately. In case of the FDF observations, the HgCd lamp has been used additionally to the He, Ar and Ne lamps to warrant better efficiency in the blue wavelength range which is particularly neccessary for the higher redshift spiral galaxies. Typical instrumental resolutions for the observed spectra fall in the range of $\sigma_i \approx 85 - 100 \, {\rm km \, s^{-1}}$. To ensure a reliable error treatment for the velocity dispersions and radial velocity measurements and to derived the signal-to-noise of each galaxy spectra Monte-Carlo simulations for different stellar templates over a range of input σ and S/N ratios were performed (Fritz 2006). For $S/N < 8$ per Å the velocity dispersions are systematically underestimated on average by 4%, but for S/N$\geq$8 per Å the effect becomes negligible. To check the reliablility and accuracy of our velocity dispersion measurements, serveral independent tests have been performed. These verifications are presented in § A of the Appendix.

An example of the velocity dispersion measurement for a field elliptical galaxy in the WHDF with typical S/N spectrum at $z = 0.2599$ is given in Figure 2. Several template star spectra were smoothed to the same resolution as the galaxy spectrum to derive σ. The velocity dispersion for this galaxy is $\sigma_f = 128 \pm 8 \, {\rm km \, s^{-1}}$ derived within the extracted spectral region around the Mg_b feature with a signal-to-noise level of $S/N = 57 \, {\rm Å^{-1}}$ (see Figure 2). In this case, the final σ_f was averaged over three individual measurements $\sigma_1 = 127 \pm 8 \, {\rm km \, s^{-1}}$, $\sigma_2 = 134 \pm 8 \, {\rm km \, s^{-1}}$ and
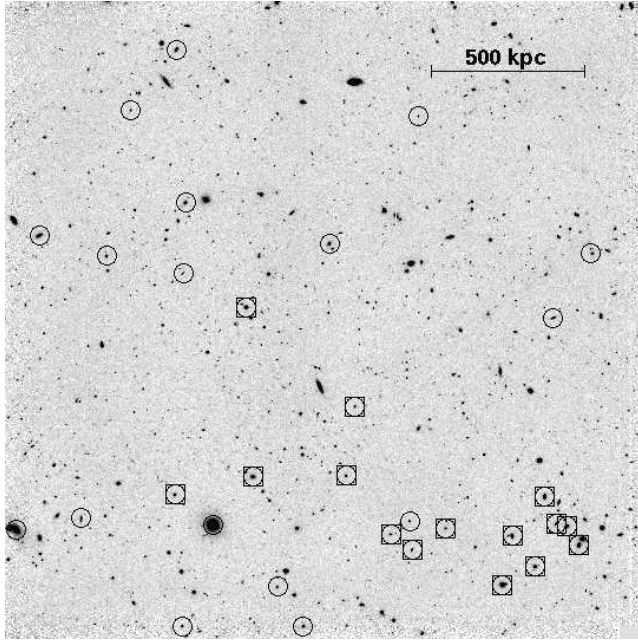
Figure 4. Distribution of the field early–type galaxies within the FDF and possible members of a cluster in the southwestern (lower right) corner. Field early–type galaxies are shown as circles, cluster early–type candidates are denoted additionally by squares. The bar corresponds to 500 kpc in projection at the cluster redshift of $z = 0.33$.

Figure 5. Distribution of the field early–type galaxies within the WHDF. The bar corresponds to 600 kpc in projection at a redshift of $z = 0.33$. The three galaxies located in the northern (upper middle) part of the WHDF are not members of a group. North is up and east is to the left.

$\sigma_3 = 124 \pm 10$ km s^{-1} which are in excellent agreement as the scatter between the values varies only within their uncertainties.

The measured luminosity–weighted average velocity dispersions $\sigma_{\rm ap}$ were aperture corrected as $\sigma = (1.15 \pm 0.04)\sigma_{\rm ap}$ (similar to Jørgensen et al. 1995, but adopting a slope of -0.06) to yield central velocity dispersions within a circular aperture of radius $R_e/8$. For each galaxy, its aperture during the observations was individually computed using the slit width, the number of extracted rows over which the spectrum was averaged and the respective pixel scale (see Fritz et al. 2005, for a description).

2.3.3 Redshift and Spatial Distribution

Figure 3 shows the redshift distribution of all spectroscopically confirmed field early–type galaxies detected within the FDF and WHDF. Early–type galaxies in the FDF that were spectroscopically identified to be members of a cluster at $z \approx 0.33$ (see next paragraph) are indicated as well. The VLT spectra of these cluster E+S0 candidates are of similar high quality to the spectra obtained for the field galaxies. The 13 field E+S0 galaxies in the FDF encompass a range in redshifts of $0.22 \leq z_{\rm FDF} \leq 0.65$ with a mean of $\overline{z}_{\rm FDF} = 0.42 \pm 0.11$ ($\langle z_{\rm FDF} \rangle = 0.41$) and the 11 field galaxies in the WHDF cover a redshift space of $0.21 \leq z_{\rm WHDF} \leq 0.74$ with a mean of $\overline{z}_{\rm WHDF} = 0.36 \pm 0.16$ ($\langle z_{\rm WHDF} \rangle = 0.40$). The total field sample of 24 E+S0 galaxies exhibits a mean redshift of $\overline{z} = 0.39 \pm 0.14$ and a median of $\langle z \rangle = 0.40$.

It turned out that the southwestern corner of the FDF most probably covers the outskirts of a galaxy cluster at $z = 0.335 \pm 0.002$ (Ziegler et al. 2005). Based on the radial velocity measurements for the elliptical galaxy candidates in the FDF, the lower limit for the velocity dispersion of the cluster is $\sigma_{\rm c} \gtrsim 430$ km s^{-1}, which is most likely only a lower limit as the cluster centre is not located on the FDF but only its outskirts. Allowing for a spread in redshift
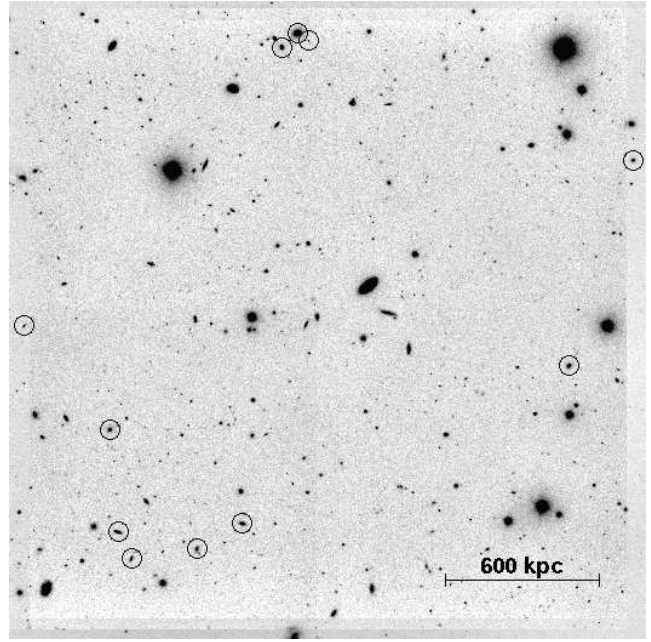
space of $\Delta z = 0.04$, which corresponds to ~ 6 times the typical velocity dispersion of a rich galaxy cluster ($\sigma_{\rm c} \approx 10^3$ km s^{-1}), it is found that a total of 13 spiral galaxies and 15 early-type galaxies based on their spectroscopic redshifts are likely to be members of this cluster. This is also visible through a small break in redshift space at $z \approx 0.3$ for the 341 galaxies at $0.1 < z < 5$ (144 with $z < 1.1$) of the total spectroscopic catalog (Noll et al. 2004).

The spatial distribution of all early-type field galaxies in the FDF is shown in Figure 4. Potential cluster members are additionally denoted by squares. Adding the possible spiral cluster candidates, it is suggestive that the cluster has an elongated shape. If the center indeed is positioned to the southwestern corner of the FDF, the distribution of the galaxies will be a striking example of the morphology–density relation (Dressler 1980) with the early–type galaxies mainly populating the dense, inner region and the late–type galaxies located at larger clustercentric radii. Unfortunately at a redshift of $z = 0.33$, the Mg 5170 absorption line is strongly affected due to the terrestrial absorption of the B band, which makes an accurate measurement of the internal galaxy velocity dispersions impossible. For this reason, early-type galaxies which are possible members of a cluster at $z \approx 0.33$ will be discarded from the further analysis. Nevertheless, these E+S0 cluster galaxies will be used as a reference for comparison reasons at a later stage, see § 5. The coordinates, redshifts and rest-frame $(B - I)$ colours of the cluster galaxies are presented in Table 4.

Figure 5 illustrates the spatial distribution of the early-type field galaxies in the WHDF. Apart from three galaxies which are located in the northern part of the image, all field ellipticals are homogenously distributed over the entire field. To test for possible group candidates, radial velocity measurements of the three galaxies close in projection resulted in a dispersion in radial velocities of $\Delta v_{\rm rad} \simeq 450$ km s^{-1} and a group velocity dispersion of $\sigma_{\rm grp} = 190^{+63}_{-71}$ km s^{-1} at $z = 0.2125$. Looking at the individual ACS galaxy images, these objects are not visually associated to

Table 5. Physical Properties of the field early-type galaxies in the FDF and WHDF. The velocity dispersions σ are not corrected for aperture. The S/N is per Å (1.6 Å pixel^{-1}). The error on M/L (in solar units) is the same as the error on the mass M.

ID	$z_{\rm spec}$	σ (km s^{-1})	S/N (Å^{-1})	$B_{\rm tot}$ (mag)	$\log R_{\rm e}$ (kpc)	$R_{\rm e}$ (arcsec)	$\langle\mu_{\rm e}\rangle_B$ (mag arcsec^{-2})	$\log M$ ($M_\odot$)	$\log(M/L_B)$ ($M_\odot/L_\odot$)	$\Delta\ln(M/L_B)$	$B-I$ (rest)
FDF-1161	0.3959	125±16	19	23.41	0.33±0.07	0.40	20.30±0.12	10.65±0.06	0.38	−0.68±0.15	1.87
FDF-4285	0.3956	159±16	29	23.19	0.33±0.07	0.40	20.30±0.13	10.87±0.05	0.51	−0.30±0.13	1.87
FDF-5011	0.6538	82±13	15	24.84	0.54±0.08	0.50	20.59±0.15	11.46±0.04	0.87	0.00±0.11	1.94
FDF-5908	0.2237	286±05	127	19.71	0.95±0.06	2.50	21.51±0.11	11.98±0.04	1.03	−0.05±0.09	1.87
FDF-6307	0.4513	185±14	29	23.52	0.53±0.07	0.59	20.79±0.08	11.21±0.05	0.74	−0.17±0.12	1.91
FDF-6336	0.4593	140±43	8	24.69	0.46±0.08	0.50	21.79±0.15	10.91±0.12	0.96	0.52±0.00	1.99
FDF-6338	0.4100	164±19	22	23.89	–	–	–	–	–	–	1.88
FDF-6439	0.3955	200±15	41	22.44	0.27±0.06	0.35	19.21±0.09	11.01±0.05	0.42	−0.76±0.12	2.07
FDF-7116	0.4567	123±21	28	24.21	0.16±0.07	0.25	19.68±0.10	10.47±0.07	0.28	−0.77±0.18	1.70
FDF-7459	0.5386	172±23	20	24.28	–	–	–	–	–	–	1.85
FDF-7796	0.4089	106±33	15	23.65	0.61±0.08	0.75	21.80±0.17	10.80±0.13	0.57	−0.34±0.31	2.02
FDF-8372	0.2290	161±09	57	21.62	0.17±0.06	0.40	19.79±0.12	10.70±0.04	0.46	−0.28±0.11	2.01
FDF-8626	0.4081	379±37	27	21.45	0.90±0.06	1.45	21.00±0.12	12.05±0.05	0.90	−0.20±0.12	1.95
WHDF-92	0.3988	183±13	31	22.53	−0.02±0.06	0.18	17.69±0.13	10.66±0.03	0.15	−1.42±0.08	2.06
WHDF-111	0.7418	172±12	23	22.88	0.82±0.05	0.91	19.93±0.13	11.46±0.04	0.16	−1.93±0.11	2.05
WHDF-158	0.4825	134±14	37	21.28	0.86±0.07	1.28	20.81±0.15	11.28±0.07	0.26	−1.57±0.16	1.85
WHDF-173	0.4507	184±16	37	22.51	0.70±0.04	0.88	20.60±0.14	11.39±0.02	0.60	−0.84±0.06	2.08
WHDF-318	0.3973	211±14	32	22.25	1.01±0.10	1.91	22.53±0.11	11.81±0.10	1.17	0.24±0.25	2.02
WHDF-437	0.2599	128±08	57	21.67	0.64±0.05	1.10	21.38±0.10	10.99±0.03	0.63	−0.52±0.09	1.89
WHDF-508	0.3977	138±39	9	–	1.19±0.10	2.92	24.33±0.20	11.64±0.06	1.35	0.72±0.15	2.01
WHDF-749	0.2130	130±11	52	21.10	–	–	–	–	–	–	2.66
WHDF-810	0.2133	186±10	83	20.28	0.73±0.07	1.54	21.14±0.09	11.40±0.07	0.77	−0.40±0.16	2.00
WHDF-946	0.2123	107±05	49	21.63	0.70±0.07	1.47	22.40±0.15	10.89±0.07	0.82	−0.05±0.16	2.07
WHDF-810b	0.2118	140±19	20	21.59	0.13±0.07	0.39	19.49±0.15	10.55±0.02	0.46	−0.65±0.06	−0.47

Table 3. Coordinates and redshifts of the field early-type galaxies in the FDF and WHDF

ID	$z_{\rm spec}$	α (J2000.0)	δ (J2000.0)
FDF-1161	0.3959	01 05 51.689	-25 45 45.965
FDF-4285	0.3956	01 06 02.961	-25 44 55.832
FDF-5011	0.6538	01 06 05.549	-25 48 48.886
FDF-5908	0.2237	01 06 08.796	-25 48 06.816
FDF-6307	0.4513	01 06 10.208	-25 44 28.225
FDF-6336	0.4593	01 06 10.334	-25 45 16.169
FDF-6338	0.4100	01 06 10.329	-25 49 15.565
FDF-6439	0.3955	01 06 10.669	-25 42 44.437
FDF-7116	0.4567	01 06 12.961	-25 43 25.565
FDF-7459	0.5386	01 06 14.172	-25 45 04.429
FDF-7796	0.4089	01 06 15.428	-25 48 02.843
FDF-8372	0.2290	01 06 17.554	-25 44 50.593
FDF-8626	0.4081	01 06 18.705	-25 48 10.266
WHDF-92	0.3988	00 22 42.293	00 18 27.750
WHDF-111	0.7418	00 22 39.393	00 18 33.610
WHDF-158	0.4825	00 22 42.873	00 18 44.700
WHDF-173	0.4507	00 22 37.386	00 18 50.560
WHDF-318	0.3973	00 22 43.251	00 19 52.580
WHDF-437	0.2599	00 22 22.977	00 20 34.840
WHDF-508	0.3977	00 22 47.040	00 21 01.450
WHDF-749	0.2130	00 22 20.162	00 22 50.460
WHDF-810	0.2133	00 22 34.984	00 24 14.120
WHDF-946	0.2123	00 22 35.664	00 24 04.960
WHDF-810b	0.2118	00 22 34.286	00 24 09.670

Table 4. Properties of identified cluster early-type galaxies in the FDF

ID	$z_{\rm spec}$	α (J2000.0)	δ (J2000.0)	$B_{\rm tot}$ (mag)	$B-I$ (rest)
FDF-822	0.3357	01 05 50.371	-25 48 19.922	23.17	2.11
FDF-980	0.3340	01 05 50.986	-25 48 07.142	24.01	2.07
FDF-1114	0.3345	01 05 51.520	-25 48 05.462	22.70	2.15
FDF-1265	0.3340	01 05 52.103	-25 47 47.219	23.33	2.12
FDF-1371	0.3356	01 05 52.579	-25 48 34.480	22.52	2.21
FDF-1697	0.3365	01 05 53.736	-25 48 13.855	22.63	2.24
FDF-1836	0.3325	01 05 54.221	-25 48 47.082	25.16	3.84
FDF-2580	0.3390	01 05 57.080	-25 48 08.880	22.67	2.18
FDF-3051	0.3335	01 05 58.775	-25 48 23.506	22.43	2.28
FDF-3365	0.3312	01 05 59.842	-25 48 13.029	23.92	2.04
FDF-3909	0.3378	01 06 01.661	-25 46 46.379	22.19	2.11
FDF-4030	0.3360	01 06 02.098	-25 47 33.302	23.48	2.18
FDF-5362	0.3318	01 06 06.786	-25 47 34.088	25.22	3.80
FDF-5446	0.3355	01 06 07.131	-25 45 39.069	23.67	1.76
FDF-6457	0.3360	01 06 10.720	-25 47 46.366	25.28	1.61

each other through tidally distorted outer structures (e.g. tidal arms, collisional rings, interaction signatures) or very nearby other companions. For this reason, both independent approaches give strong evidence that the three objects are not likely members of a group but isolated field galaxies.

The coordinates and redshifts of the galaxies for which velocity dispersions were measured are given in Table 3. Velocity dispersions, S/N ratios, total Johnson B-band magnitudes, sizes, sur-

Table 6. HST/ACS F814W observations of the FDF and WHDF

Field	Date	Area arcmin^2	$T_{\rm tot}$ [sec]	M$_{\rm lim}$ 3σ
FDF	20/07-29/09/02	6.8×6.8	2360	25.50
WHDF	14/08-23/08/03	6.8×6.8	2450	26.30

face brightnesses, dynamical masses, M/L ratios, and rest-frame $(B - I)$ colours of the galaxies are presented in Table 5.

2.3.4 Spectroscopic Star Formation Signatures

To estimate the amount of recent star formation present in our field galaxies we measure the spectral diagnostic features of [O II] $\lambda3727$ and H$\delta_A\lambda4101$ in the observed wavelength range of the spectra. For the indices [O II] $\lambda3727$ and H$\delta_A\lambda4101$ we adopt the passband definitions by Balogh et al. (1997) and Worthey & Ottaviani (1997), respectively. Uncertainties in the line index measurements account for poisson noise as well as possible noise variations in the spectra. In the subsequent analysis we always refer to rest-frame equivalent widths in units of Å. The spectroscopic measurements of our galaxies will further be discussed in § 5.2, where the implications of the recent activity signatures on the stellar population properties will be assessed.

3   PHOTOMETRY

3.1   HST/ACS Observations

Using the Advanced Camera for Surveys (ACS) Wide Field Channel (WFC), *Hubble Space Telescope (HST)* observations of the FORS and William Herschel Deep Fields were carried out during cycles 11 and 12. To cover the $\sim 7 \times 7$ arcmin^2 sky areas of the FDF and WHDF, four WFC pointings were aligned as a 2×2 mosaic. A single ACS WFC chip offers a field–of–view of $\sim 202 \times 202$ arcsec^2 and a pixel scale of $\sim$0.049 arcsec. Each pointing was split into two exposures and has a total exposure time of 2360 s (FDF) and 2450 s (WHDF) through the F814W (I) filter. Table 6 gives an overview of the HST/ACS observations of the FDF and WHDF. The column $T_{\rm tot}$ represents the total exposure time for each object and M$_{\rm lim}$ lists the 50% completeness limit for 3σ detections of extended sources within the two deep fields. Data reduction was performed using the standard CALACS [2] pipeline and the unprocessed images (including bias and dark subtraction, flat–fielding, distortion and astrometric correction) were used for an additional cosmic ray rejection filtering by combining the two exposures of each visit to produce the final mosaic.

3.2   Surface Photometry

Structural parameters of half-light (effective R_e) radii, (effective) surface brightnesses ($\langle\mu_e\rangle$ within R_e) and total magnitudes and shapes of the galaxies were derived with the GALFIT package (Peng et al. 2002). For the convolution of the surface brightness

[2] http://www.stsci.edu/hst/acs/analysis

model profiles, an average PSF was constructed using ~ 20 unsaturated stars with $I_{814} < 23$ which were normalized to the same central flux and afterwards median–averaged. Two-dimensional surface brightness profiles of the galaxies were analysed with four different fitting functions, by a pure classical de Vaucouleurs $r^{1/4}$, a pure Sérsic (1968) with variable Sérsic exponent n ($1 \leq n \leq 4$), and each of those profiles in combination with an exponential disc component. The best fit to the observed light distribution of a galaxy was assessed by comparing the residual images and reduced χ^2 values. Note that by definition a profile consisting of a Sérsic plus disc component results in lower χ^2 numbers than using a single $r^{1/4}$ model alone. Therefore, preference was given to those model profiles with yielded to the lowest residual structures in the residual images. In 40% of the cases this was a pure classical de Vaucouleurs profile, in 60% of the cases this was a Sérsic plus disc component. Figure 6 presents examples of the results of the surface brightness modelling for our field galaxies. For each galaxy, the original image, the best 2D model fit and the residuals from an $r^{1/4}$ or $r^{1/n}+$ exponential disc component are shown. For internal consistency, the surface brightness distribution of the field galaxies were also modelled with the GIM2D package by Simard et al. (2002) and the algorithm by Saglia et al. (1997). A detailed discussion on differences between these techniques can be found in Fritz et al. (2005) and Ziegler et al. (2005). Total magnitudes derived with all three methods agree well within the errors as well as with those values measured on the ground-based I-band images of the FDF and WHDF with the SExtractor package. Observed magnitudes of the galaxies were calibrated on to the Vega system using the the synthetic transformation by Sirianni et al. (2005):

$$\text{TMAG} = -2.5 \times \log(\text{DN}s^{-1}) + c_0 + c_1 \times \text{TCOL} + c_2 \times \text{TCOL}^2, (1)$$

where the first term is the observed magnitude expressed as total count rate per electrons and seconds in the source system, TMAG and TCOL being the observed magnitude in the target system and the c_0, c_1, and c_2 the transformation coefficients. We adopt our $(R - I)$ aperture colors and for the coefficients $c_0 = 25.478$, $c_1 = 0.042$, and $c_2 = 0.012$. For the FDF and WHDF a galactic absorption of $E(B - V) = 0.018^m$ and $E(B - V) = 0.025^m$ was derived, respectively. Aperture colours were measured on the ground-based $UBgRI$ and BRI band photometry within a $2''$ diameter aperture.

3.3   Morphologies

Galaxy morphologies were classified using a combination between a visual inspection by one of us (A.F.), the results of the surface brightness profile analysis (i.e. interpreting the residuals from the $r^{1/4}$ luminosity profile fitting) and an independent analysis using GIM2D (see Fritz et al. 2005, for a description). The information of all three independent approaches was combined to yield the best and most reliable decision on the final morphologies of the galaxies. Figure 7 and Figure 8 display HST/ACS thumbnail images in the F814W filter of the FDF and WHDF field early-type galaxies, respectively. Table 7 and Table 8 list the morphologies and noteworthy remarks of special features for the individual galaxies. The first column of each table shows the galaxy ID, the second indicates the galaxy morphology and the last column gives additional information about special features to the respective galaxy. In total, the sample is divided into 13 field ellipticals (E and E/S0) and nine field lenticulars (S0 to Sa bulges). The two classes comprise the sub-types of 6 E, 1 E/S0, 3 S0 and 2 Sa bulges in the FDF, and 4 E, 2 E/S0, 1 S0, 1 S0/Sa and 2 Sa bulges in the WHDF. No
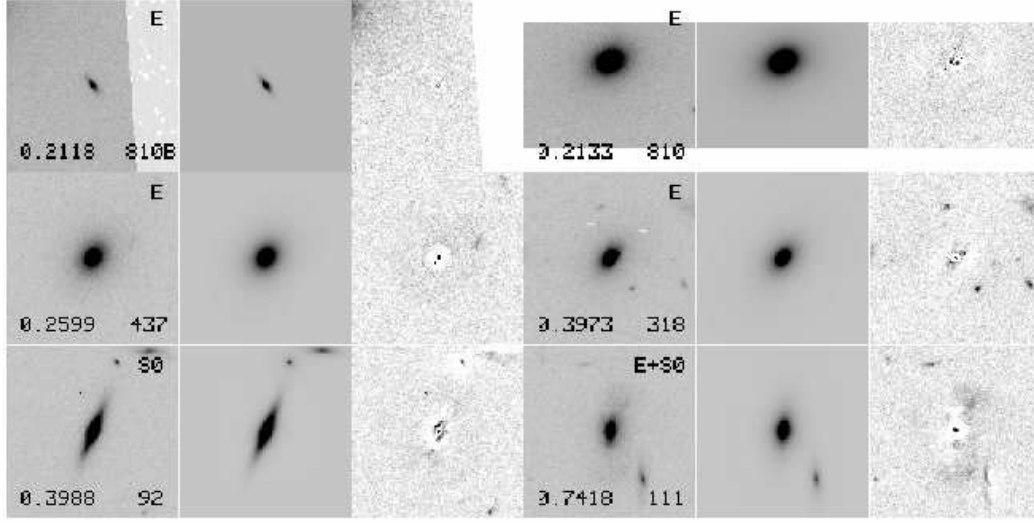
Figure 6. Examples of the surface brightness modelling using a de Vaucouleur profile for the field galaxies in our sample in order of increasing redshift. In case of object ID 92, a combination of a Sérsic plus exponential disc component yielded the best result. For each galaxy the distortion corrected original image is shown alongside the best $r^{1/4}$ model and the residuals from the respective model. Redshift, galaxy ID and morphological type classification are listed for all objects in the lower left, lower right and upper right corner. The HST/ACS F814W images are $10''$ on each side, north is up and east is to the left.

Table 7. HST/ACS morphologies and features of galaxies in the FDF

ID	morp	Note
1161	S0	
4285	E	galaxy with dust lane, merger of S0 & S?
5011	E	
5908	E	
6307	E	model too boxy, residuum at core
6336	Sa	Sb?, peculiar structure, warps
6338	S	no ACS image, no analysis, morph based on spec
6439	S0	
7116	E	hot pixel
7459	E	no analysis
7796	Sa	peculiar structure, SF in upper spiral arm?, warps
8372	S0	hot pixel
8626	E/S0	close to edge of chip

Table 8. HST/ACS morphologies and features of galaxies in the WHDF

ID	morp	Note
92	S0	two background? objects in south
111	E/S0	external halo in upper north part, two objects in north-west
158	Sa	
173	S0	
318	E	close to star, star in center
437	E	face on, faint star in north-east, [O II] 3727 emission
508	Sa	peculiar, dust pattern?, rot.?, [O II] 3727 emission?, star
749	E/S0	no ACS image, morphology based on spectrum
810	E	boxy isophotes, stars in center, [O II] 3727 emission
810b	E	discy structure, faint, [O II] 3727 emission
946	S0/Sa	lensed object (maybe in projection) in north-east

ACS image is available for the galaxy ID 6338 in the FDF, based on its spectrum this object has a morphology of a spiral galaxy (see also Table 7). The findings from the luminosity profile fitting provided a consistency check for the visual inspection and resulted in the same classification scheme except for one field galaxy in the WHDF, ID 810b: S0 (visual), E (model fit).

3.4 Spectrophotometric Properties

k-corrections were calculated by convolving respective filter transmission curves with the redshifted Spectral Energy Distribution (SED) of an early-type galaxy template from Kinney et al. (1996) as described in Fritz et al. (2005) and Fritz (2006). No separation between elliptical and S0 types was done because both exhibit similar (optical and UV) spectral shapes, Balmer discontinuities (4000 Å) and absorption features for $\lambda > 5000$ Å which are indistinguishable from their broadband optical and near-infrared colours. For internal consistency, synthetic spectral SED templates of an

12 Gyr elliptical galaxy which were generated through evolutionary synthesis modelling by Möller et al. (2001) were also utilised. Typical deviations in the k-corrections between the SEDs of the two template libraries are small $\Delta \overline{k}_B \leq 0.1^m$. Depending on the redshift of the object the most suitable filter was chosen to transform to rest-frame Johnson B-band. The B_{fors} filter was selected for galaxies in the FDF with $z > 0.25$, g_{fors} for $0.25 \leq z < 0.55$ and R_{fors} for $0.55 \leq z < 0.7$. For field objects in the WHDF with $z > 0.25$ a transformation to B rest-frame was conducted based on the B passband and for $0.55 \leq z < 0.75$ the R_C filter was utilised. Therefore, the k-correction was much less sensitive to spectral type than using a global filter transformation that is restricted to a specific filter, e.g. of $B_{\mathrm{obs}} \rightarrow B_{\mathrm{rest}}$. For reasons of consistency, the rest-frame magnitudes were checked by transforming the observed F814W-magnitudes into rest-frame Johnson-B. Deviations between magnitudes were small (differences were less than their errors). Total errors on the absolute B-band magnitudes for the galaxies were computed as the quadratic sum of individual errors in the respective ground-based photometry filter (either B, R
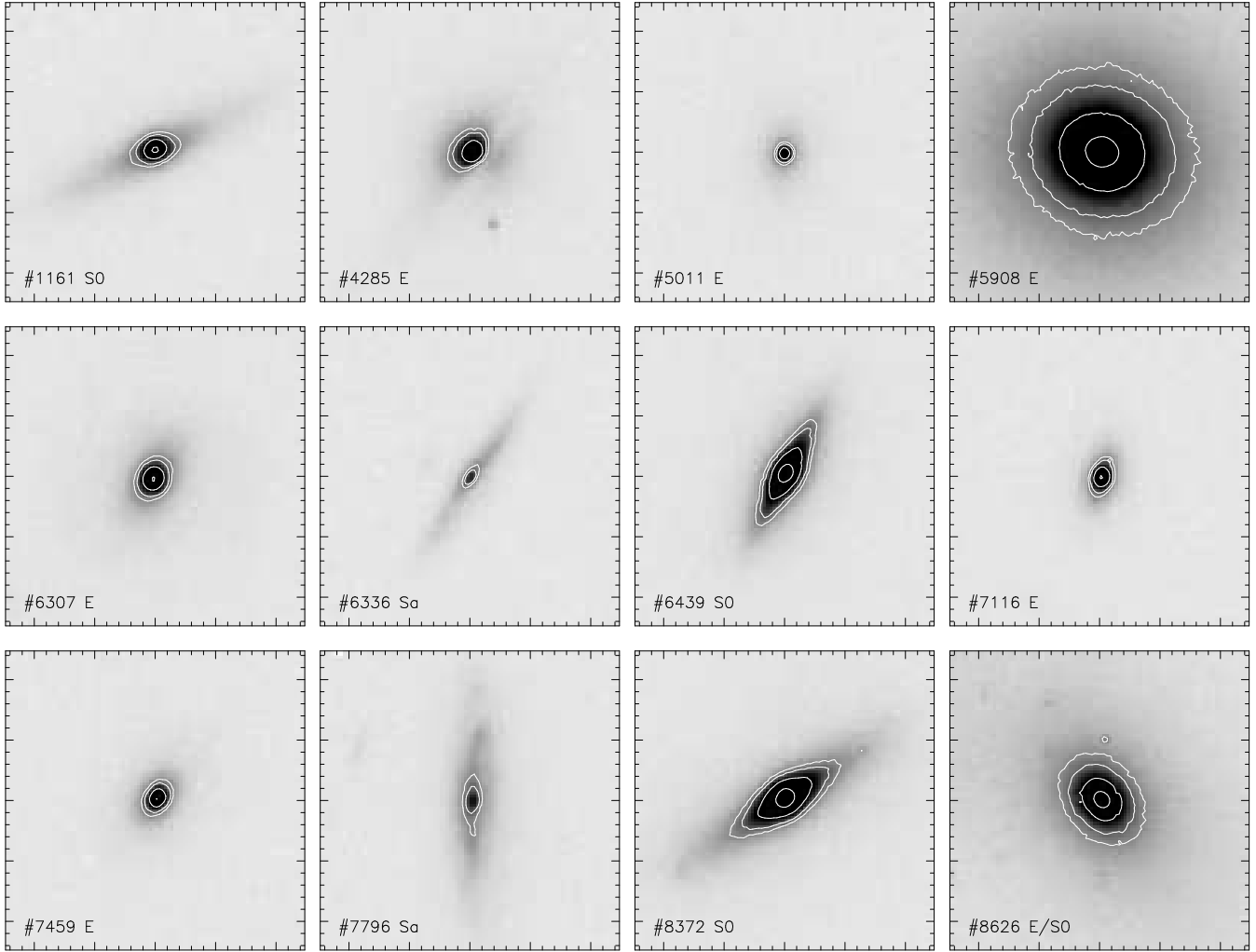
Figure 7. $5'' \times 5''$ HST/ACS F814W images of 12 FDF galaxies with available spectroscopic information. North is up and east is to the left. Isophotal contours are logarithmically displayed across the range $18.80 \leq C_i \leq 21.20$ mag arcsec^{-2}. The labels give the galaxy ID and the morphological type classification as listed in Table 7.

or I-band), the error in the k-correction and the uncertainty in the galactic absorption correction. Thanks to the very deep imaging of the FDF and WHDF, the photometric errors in the ground-based photometry are very small for all filter passbands (median uncertainties $< 0.015^m$). For the FDF and WHDF field sample, the total absolute error falls into the range $0.08^m \leq \delta M_B \leq 0.20^m$ with a median of 0.15 mag. In Figure 9 the distribution of the early-type field galaxies in the FDF and WHDF in absolute Johnson B-band magnitude are shown. Only the rest-frame magnitudes derived with the FDF and WHDF photometry are shown. The 24 E+S0 field galaxies cover a range in absolute B-band magnitude of $-22.78 \leq M_B \leq -19.40$ ($\langle M_B \rangle = -20.42$). The dashed arrow corresponds to the mean value ($\overline{M}_B = -20.68$), whereas the median is denoted by the solid arrow.

3.5 X-Ray Properties

To acquire independent complementary information on nuclear activity in our early-type galaxy sample we checked the archive for possible X-ray counterparts of our field galaxies. In the selection process of a suitable sky area for the FDF, one particular constraint
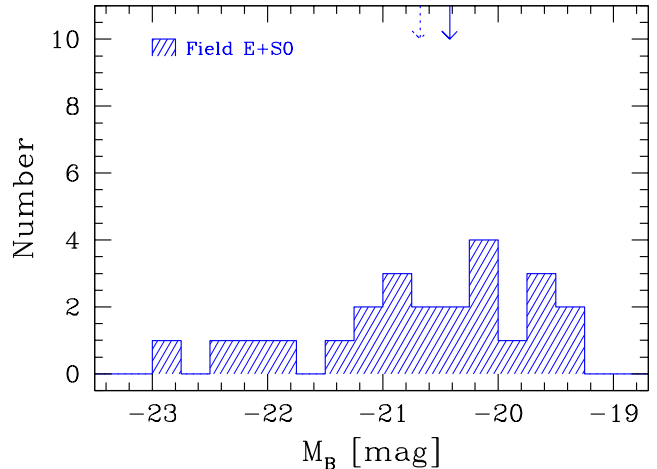

Figure 9. Absolute B-band magnitude distribution of 24 early-type field galaxies in the FDF and WHDF. Rest–frame magnitudes were derived based on the FDF and WHDF photometry. The dashed and the solid arrow give the mean ($\overline{M}_B = -20.68$) and the median ($\langle M_B \rangle = -20.42$) values of the distribution, respectively.
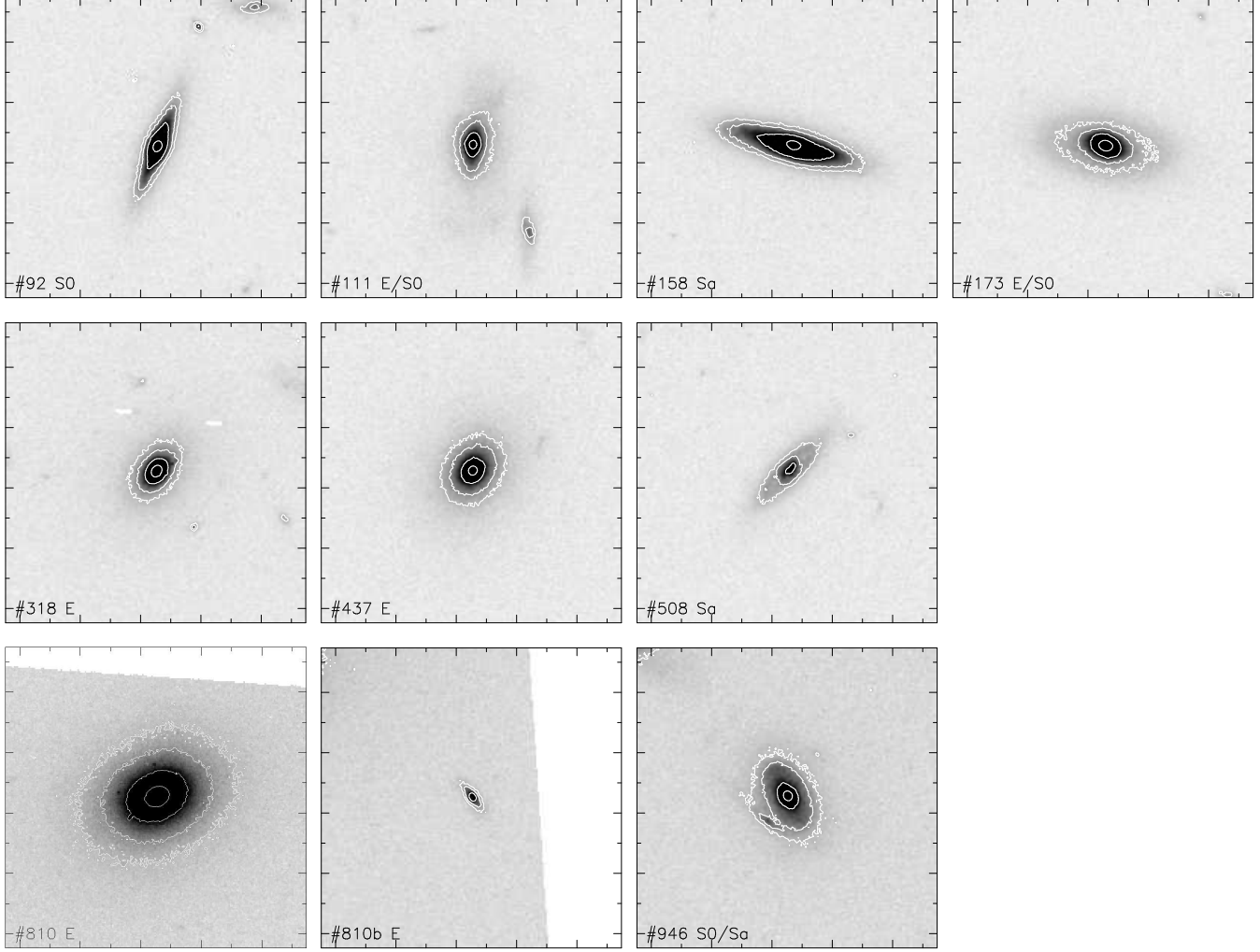
Figure 8. $10'' \times 10''$ HST/ACS F814W images of 10 WHDF galaxies with available spectroscopic information. North is up and east is to the left. Isophotal contours are logarithmically displayed across the range $18.80 \leq C_i \leq 21.20$ mag arcsec^{-2}. The labels give the galaxy ID and the morphological type classification as listed in Table 8.

was that the field had to be devoid of strong radio and X-ray sources to avoid potentially present galaxy clusters at medium redshifts. The *Chandra* and *XMM-Newton* observatories have not observed the sky region covered by the FDF; therefore, we cannot look for the presence of possible active galactic nuclei (AGNs) in these field galaxies.

For the WHDF two *Chandra* surveys are available (PI: T. Shanks, PID 02900499). A deep, high resolution ACIS-I imaging survey (72.13 ksec) of the central field and a shallow survey (10 fields with exposure times of 10 ksec each) with the ACIS-S around narrow line galaxies that have previously been detected by ROSAT. The ACIS-I covers the spectral range between 0.2 to 10 keV and has a spatial resolution of $\sim 0.492''$ or better, with PSF variations less than $0.2''$ across the total $16.9' \times 16.9'$ field-of-view (Weisskopf et al. 2002). Through a cross-correlation with our optical photometry we identified 28 objects as X-ray point-sources above a 2σ source detection limit (95% confidence level). The detected counts for each source were converted into fluxes, assuming a power law of the photon spectral flux distribution of $dN/dE \propto E^{-\Gamma}$ with an intrinsic photon index of $\Gamma = 2$ and column density of the galactic absorption of $nH = 1.0 \times 10^{21}$ cm^{-2}. A photon index of $\Gamma = 2$ is typical for X-ray emis-

sion that has its origin from star formation. The on-axis sensitivity limits of the (unabsorbed) flux in the soft ($0.5 - 2.0$ keV) and hard ($2.0 - 8.0$ keV) bands are 7.5^{-16} ergs cm^{-2} s^{-1} and 1.9^{-15} ergs cm^{-2} s^{-1}, respectively. These fluxes correspond to a detection limit in X-ray luminosities emitted in the soft band of $L_X(0.5 - 2.0\,\mathrm{kev}) = 1.9 \times 10^{42}$ ergs s^{-1} and in the hard band of $L_X(2.0 - 8.0\,\mathrm{kev}) = 4.7 \times 10^{42}$ ergs s^{-1}. The *Chandra* exposures are deep enough to both fully resolve the X-ray background (XRB) at about 1.5^{-15} ergs cm^{-2} s^{-1} in the $2.0 - 7.0$ keV energy band and detecting all the hard X-ray sources within the WHDF.

Very recently a shallow *XMM-Newton* survey (PI: M. Guainazzi, PID 0407030101) targeted a similar sky region (27.91 ksec). However, these observations cover only the southern part of the WHDF and are at a significantly coarser angular resolution of $\sim 15''$ than the *Chandra* detections. Using the same photon spectral flux distribution configuration as above the sensitivity limits of the (unabsorbed) flux in the $0.5 - 2.0$ keV energy band are 9.3^{-15} ergs cm^{-2} s^{-1} and in the $2.0 - 8.0$ keV range 2.6^{-14} ergs cm^{-2} s^{-1}. The soft and the hard fluxes correspond to detection limits of $L_X(0.5 - 2.0\,\mathrm{kev}) = 2.3 \times 10^{43}$ ergs s^{-1} and $L_X(2.0 - 8.0\,\mathrm{kev}) = 6.5 \times 10^{43}$ ergs s^{-1}. Figure 10 shows the distribution of *Chandra* and *XMM-Newton* detections in the WHDF.
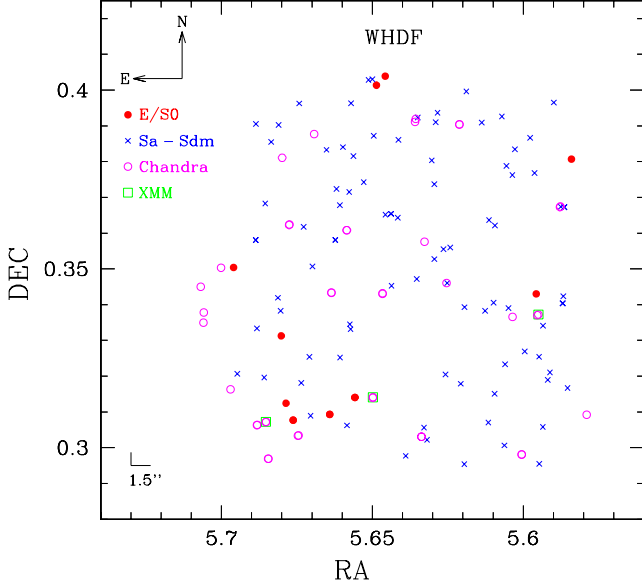
Figure 10. Distribution of *Chandra* and *XMM-Newton* detections within the WHDF. North is up and east is to the left. Early-type field galaxies in our sample are indicated as red circles. The error bars in the left correspond to 1″.5 on the respective axes.

Table 9. Galaxies with possible Chandra/XMM counterparts in the WHDF

ID	morp	Chandra / XMM	association	Note
92	S0	yes? / no	maybe	XMM bright, extended
158	Sa	no / yes?	not likely	XMM bright, extended
173	S0	yes? / yes?	likely	XMM bright
437	E	yes? / yes?	maybe	[O II] emission
438	Sc	yes / no	yes	$z = 0.0473$, no $V_{\max}$
635	Sc	yes / no	yes	$z = 0.0709$, no $V_{\max}$

Three galaxies that were observed by *Chandra* were additionally detected by us on the *XMM* images (see Figure 10). Apart from two clear Chandra detections of two Sc spiral galaxies (ID 438) at $z = 0.0473$ and (ID 635) at $z = 0.0709$ (no maximum rotation velocity $V_{\max}$ could be derived for both objects), four field early-type galaxies might have associated X-ray counterparts. These objects in the WHDF with possible Chandra and/or XMM counterparts are listed in Table 9. There is only one rather likely candidate for a galaxy with a central AGN (ID 437) as this object shows also weak [O II] emission. In case of the other candidates either bright (ID 173) or bright and extended (ID 92 or 158) *XMM* sources close to the galaxies are found that might be associated to the optical counterparts. Non of the early-type galaxies in our sample is surrounded by a diffuse halo-gas, thus no object appears to be an extended X-ray source, hence the influence of AGN activity for our galaxies is small or even negligible. We will discuss the possible impact of X-ray detections together with our results in section 7.1. In Appendix § B, we assess in more detail contributions due to low-luminosity AGN (LLAGN) and/or emission from soft, diffuse X-ray plasma or or low-mass X-ray binaries (LMXBs) in case of our galaxies.

4   SCALING RELATIONS OF FIELD EARLY–TYPE GALAXIES AT Z=0.4

4.1   The Local Reference

To derive the kinematic and/or the spectrophotometric evolution of early-type galaxies at intermediate redshift, it is crucial to carefully select a sample of early-type galaxies at low redshift which can be utilised as a reference for the purpose of comparison. The Coma cluster at $z = 0.024$ is one of the best studied local rich clusters of galaxies and represents with a look–back time of only $\sim$0.3 Gyr (corresponding to 2% of the age of the Universe) the present-day Universe. A number of previous works in the literature on both cluster and field early-type galaxies (e.g., van Dokkum & Franx 1996; Treu et al. 2001, 2002, 2005; van de Ven et al. 2003; Jørgensen et al. 2006) used this cluster for the purpose of comparison of the Fundamental Plane at $z > 0.1$ and it therefore provides a reliable and widely accepted local reference when addressing evolutionary questions.

In order to minimise systematic uncertainties arising from filter transformations, distance determinations and selection effects, we utilise the well defined Coma sample in the Johnson B-band by (Saglia, Bender & Dressler 1993, hereafter SBD93) which comprises 39 early-type cluster galaxies (splitted into 25 E and 14 S0s). This data compilation is a sub–set of the original "7 Samurai" sample (Faber et al. 1989) which contains 59 E+S0 galaxies in the Virgo and Coma cluster; but for the latter no morphological information is available. For deriving the evolution of the M/L with redshift we use the FP coefficients as published by Faber et al. (1989).

4.2   The Faber–Jackson Relation

Early-type galaxies follow a scaling relation between their luminosity and internal velocity dispersion, also known as the Faber–Jackson relation (Faber & Jackson 1976). The relationship can be used to constrain the formation and evolution of E+S0 galaxies but it requires accurate velocity dispersion measurements as small uncertainties in the kinematics transfer into large errors in the magnitudes, hence the measured luminosity evolution.

Figure 11 shows the Faber–Jackson relation (FJR) in the B-band for the field early-type galaxies in the FDF and WHDF, compared to the local Coma sample by SBD93. For this scaling relation, galaxy magnitudes were measured with SExtractor on the deep ground-based images with $\sim$0.60 arcsec FWHM in the I-band, hence the whole field sample can be considered. As the median uncertainty in our velocity dispersion measurements is only 15 km s^{-1} and our magnitude limit reaches $M_B = -19.30$ (about one magnitude fainter than previous studies), we can put reliable implications on the evolution of our distant field galaxies using the FJR. A linear χ^2-fit to the restricted Coma reference sample yields:

$$M_B = -1.22 \log \sigma - 8.31, \qquad (2)$$

which is indicated as a dashed line in Figure 11. Assuming that the local slope holds valid for our distant galaxies (i.e. there is not evolution in the slope of the FJR), we analyse the mean residuals from the local FJR, shown as the solid line in Figure 11. Because of the on average younger light-averaged ages of the stellar populations in the distant galaxies, for a given velocity dispersion the field galaxies are on average brighter by $\Delta M_B = -0.65 \pm 0.16$ mag (median $\Delta \langle M_B \rangle = -0.44$ mag) than their local counterparts. The $\pm 1\sigma$ scatter of the offsets in the FJR for the distant
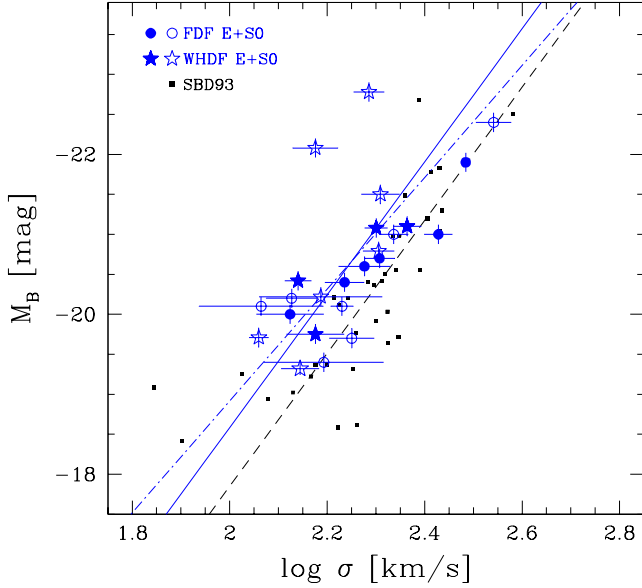
Figure 11. Faber–Jackson relation for the early-type field galaxies in the FDF and WHDF, compared to the Coma galaxies of SBD93 (small squares) in rest-frame Johnson B-band. The dashed line shows the χ^2-fit to the local restricted FJR by SBD93 (within selection boundaries defined by the distant galaxies), the dot-dashed line indicates an unconstrained χ^2-fit to the distant sample. The average evolution of the distant field galaxies of $\Delta\langle M_B \rangle = -0.44$ mag with respect to the local galaxies is shown by the solid line.

Figure 12. Faber–Jackson relation for the early-type field galaxies in the FDF and WHDF in the rest-frame K-band. Large symbols are the field early-type galaxies, open squares are local cluster early-type galaxies from Pahre (1999). The Faber-Jackson relation of the distant field early-type galaxies has a similar scatter as the local relationship. An average evolution of $\Delta\langle M_K \rangle = -0.59$ mag for the distant galaxies with respect to the local reference is found, indicated by the solid line. An unconstrained χ^2-fit to the distant sample is shown by the dot-dashed line.

galaxies is $\sigma_r = 0.72^m$. The two objects that are slightly offset from the rest of the distant field galaxies show both signs of star formation, one of them being also the galaxy with the highest redshift in our sample (cf. § 5.2). The measured evolution is in very good agreement with a slow, passive evolution of the stellar populations as suggested by single-burst simple stellar populations models with a high formation redshift of the bulk of the stars (Bruzual & Charlot 2003). For formation redshift of $z_f = 2$ these evolution models predict an average increase in the Johnson B-band of 0.61 ± 0.06 mag at $z = 0.4$. Similar as for local studies, our distant galaxies show weak evidence for a larger scatter at fainter luminosities ($M_B > -20.40$), that might be indications for an evolution of slope in the FJR. We interpret this effect as a stronger evolution of the lower-mass galaxies. However, apart form the mass dependence, an additional small contribution to the offset of lower-luminosity galaxies might be the result of a weak dependence of the velocity dispersion on luminosity of the early-type galaxies that was previously found within a large sample of early-type galaxies drawn from Data Release 4 of the Sloan Digital Sky Survey (SDSS, Desroches et al. 2007). This luminosity dependence becomes detectable in all FP projections and is most pronounced for faint galaxies in the SDSS around $M_r = -21.2$ which corresponds to about $M_B = -20.2$. At $M_B = -20.3$ our field distant galaxies show a diversity, half of the sample indicates a strong luminosity evolution whereas the other half a mild evolutionary trend. An un-constrained linear χ^2-fit to our field galaxy sample yields:

$$M_B(z = 0.4) = -4.93 \log \sigma - 6.99. \tag{3}$$

However, our sample is too small and the dependence on luminosity too weak to test possible luminosity effects on the slope of the FJR at $z = 0.4$ in greater detail.

To verify our results and to test the underlying stellar populations in even more detail, we converted the extinction-corrected
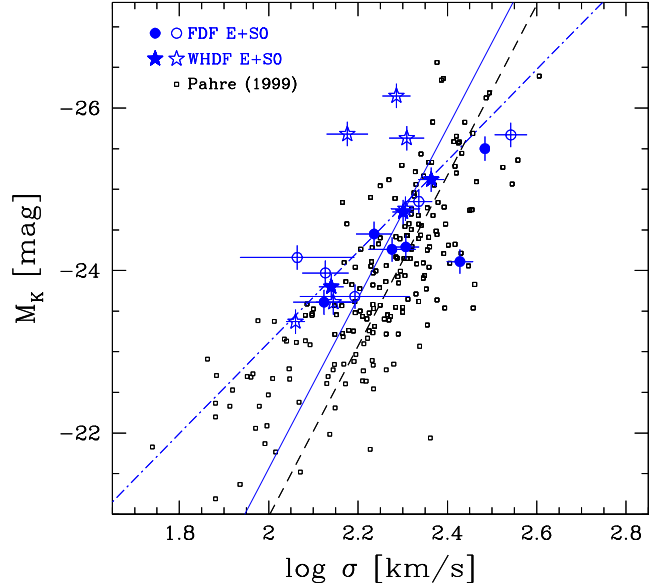
$(B - R)$ rest–frame colors of the field galaxies in our sample into M/L ratios in the K-band following a similar approach as in Bell & de Jong (2001). Absolute K-band magnitudes were derived by using the synthetic stellar population models by Möller et al. (2001). The FJR in the K-band for the field E+S0 galaxies in the FDF and WHDF is presented in Figure 12. The early-type galaxies are compared to the local relationship of cluster early-type galaxies as found by Pahre (1999). For a given velocity dispersion the luminosities of the distant field galaxies (excluding ID 111 at $z = 0.7418$) are on average brighter by $\Delta M_K = -0.68 \pm 0.21$ mag (median $\Delta\langle M_K \rangle = -0.59$ mag) than their local representatives. The moderate luminosity evolution found for the field E+S0 is in excellent agreement to the findings derived using the B-band magnitudes. Less-massive galaxies display a larger offset with respect to the local relationship, confirming the faster evolution of less-massive galaxies in the B-band. Furthermore, lower-luminosity (mass) galaxies show a faster evolution in luminosity than higher-luminosity (mass) galaxies. This point will be addressed in greater detail in § 5.

4.3 The Kormendy Relation

To study the change of surface brightness evolution for the FP sample at a fixed size, the magnitude–size relation was constructed. The Kormendy relation (KR) represents the projection of the Fundamental Plane along the velocity dispersion onto the photometric plane. As only the structural parameters are used, samples have larger scatter in the KR than in the FP but results should complement and endorse findings obtained with the FP.

The KR of the field galaxies is presented in Figure 13. For a given size the surface brightnesses of the distant field galaxies (excluding the Sa ID 508) are on average brighter by $\Delta\mu_{e\,B} =$
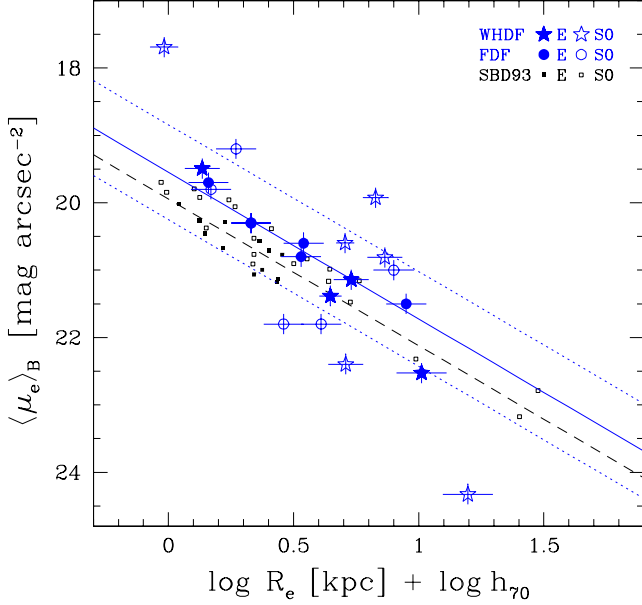
Figure 13. Kormendy relation for the early-type field galaxies in the FDF and WHDF compared to the Coma galaxies of SBD93 in rest-frame B-band. The dashed line shows the χ^2-fit to the local KR by SBD93. The average evolution of the distant field galaxies with its scatter with respect to the local galaxies is shown by the solid and dotted lines, respectively.

-0.40 ± 0.39 mag arcsec^{-2} (median $\Delta\langle\mu_e\rangle_B = -0.51$ mag arcsec^{-2}). One object (ID 508) that does not follow the KR is a spiral galaxy, has a high surface brightness and also shows possible signs of rotational support in its two-dimensional spectrum (cf. § 4.4). We confirm the power of the KR to separate passive quiescent galaxies from galaxies with blue colors as found by Ferreras et al. (2005). In consistency with passive evolution models, the fading of the stellar populations implies that the galaxies will evolve to brighter surface brightnesses with increasing redshift, hence moving away from the local KR of present day early-type galaxies.

There are no indications of an evolution in the sizes of our field galaxies, see Figure 13. We emphasise that it is hard to separate an evolution in the size of the galaxies from an evolution in the surface brightness as the photometric parameters of half-light radius and surface brightness are correlated and enter the FP and its projections in combination as $FP_{\mathrm{phot}} = \beta\,\mu_e + \log R_e$, with $\beta = 0.328$ (e.g., Saglia et al. 1997; Fritz et al. 2005). The measurements and results derived for the KR depend critically on the selection procedures applied to the sample galaxies. For example, two studies targeting the same sky region obtained inconsistent results, di Serego Alighieri et al. (2005) claims an evolution in the size of galaxies in the CDFS whereas van der Wel et al. (2005) does not support this finding. Most likely this effect is due to differences or constraints set in the selection process, where the former primarily selected fainter objects whereas the latter observed a more homogenous population of early-type galaxies. In case of the low-mass galaxies a differential evolution can be produced by a combined effect of large spectroscopic apertures and substantial rotational support in the target objects. In particular, the combination of the large slit-apertures with low S/N galaxy spectra by di Serego Alighieri et al. (2005) can cause miss-classifications of spirals with unresolved possible rotational support as detectable in the emission lines. This effect points to a bias in the selection proce-

dure. A further discussion on possible selection effects is presented in § 6.

4.4   The Fundamental Plane

Early-type galaxies in the nearby Universe follow a tight fundamental relationship which is defined by their basic observables as

$$\log R_{\mathrm{e}} = \alpha \log \sigma + \beta \log I_{\mathrm{e}} + \gamma, \qquad (4)$$

where R_{e} is the effective (half-light) radius given in kpc, σ denotes the internal velocity dispersion in km s^{-1} and I_{e} is the surface brightness in mag arcsec^{-2}, related to $\langle\mu_{\mathrm{e}}\rangle$ as $\log I_{\mathrm{e}} = -0.4\langle\mu_{\mathrm{e}}\rangle$. For the FP coefficients we performed a principal component analysis and derived for the slopes and the intercept $\alpha = 1.25$, $\beta = -0.82$ and $\gamma = -9.0$, which are in good agreement with the FP coefficients by SBD93; Jørgensen et al. (1996). From the sample of field galaxies of Faber et al. (1989) we measured that the intercept of the FP is offset by $\Delta\overline{\gamma} = 0.04$ from the relation as given in equation 4.

Figure 14 shows the FP for the 21 early-type field galaxies in the FDF and WHDF in the rest-frame Johnson B-band, compared to the 39 early-type galaxies in the Coma cluster by SBD93. The local reference is indicated with small squares, whereas the distant field galaxies are shown as the large circles and stars. Filled symbols denote ellipticals, open symbols S0 galaxies and Sa bulges. The 21 FDF and WHDF early–type field galaxies are morphologically classified into 9 E and 12 S0. Five ellipticals and six S0s originate from the FDF and four Es and six S0s are located in the WHDF. Two galaxies are not visible on the ACS images and for one elliptical galaxy in the FDF no structural parameters could be derived. The distant field galaxies cover a redshift range of $0.21 \leq z_{\mathrm{Field\,E}} \leq 0.74$ with a median of $\langle z_{\mathrm{Field\,E}}\rangle = 0.40$. Two outliers in the FP, ID 6336 ($\log R_{\mathrm{e}} = 0.46$) and ID 508 ($\log R_{\mathrm{e}} = 1.20$), reveal on the ACS images a significant disc component and early spiral morphology. Galaxy ID 6336 has an extraordinary strong Hδ_{F} absorption, which points to a young luminosity-weighted average model age under assumption of a single stellar population. On the ACS images, ID 508 shows a peculiar structure which might indicate that this object is an ongoing merger. Both galaxies were classified as Sa bulges hence these early-type spirals offer at least a low level of star formation which increases their total luminosity and displaces their position beyond the tight plane as established by early–type galaxies.

Rejecting the two outliers, for the total sample of 19 early-type field galaxies in the FDF and WHDF an average luminosity evolution of $\Delta M_B = -0.53 \pm 0.13^m$ with a median of $\Delta\langle M_B\rangle = -0.39$ is found. Similar results are measured for 17 cluster ellipticals at $\langle z\rangle \sim 0.4$ (Ziegler et al. 2005; Fritz et al. 2006) with similar look-back times ($\sim$5 Gyr), which show an average brightening of their stellar populations of $\Delta M_B = -0.44 \pm 0.18^m$, compared to their local counterparts. Overall, the distribution along the FP and the measured luminosity evolution is similar for cluster and field galaxies at $\langle z\rangle \sim 0.4$ and within the cluster sample no differences between ellipticals and S0 galaxies were found. However, the sample of distant cluster galaxies lacks galaxies with small sizes and has a magnitude limit of $M_B \leq -20.50$, whereas the field galaxy sample comprises no ellipticals with large sizes (i.e. cD galaxies) and is more than one magnitude fainter ($M_B \leq -19.30$). A comparison of the sizes and luminosities of these two data sets is therefore not adequate and would cause misleading results. Table 10 gives a summary of the results for the FP of our early-type field galaxies.
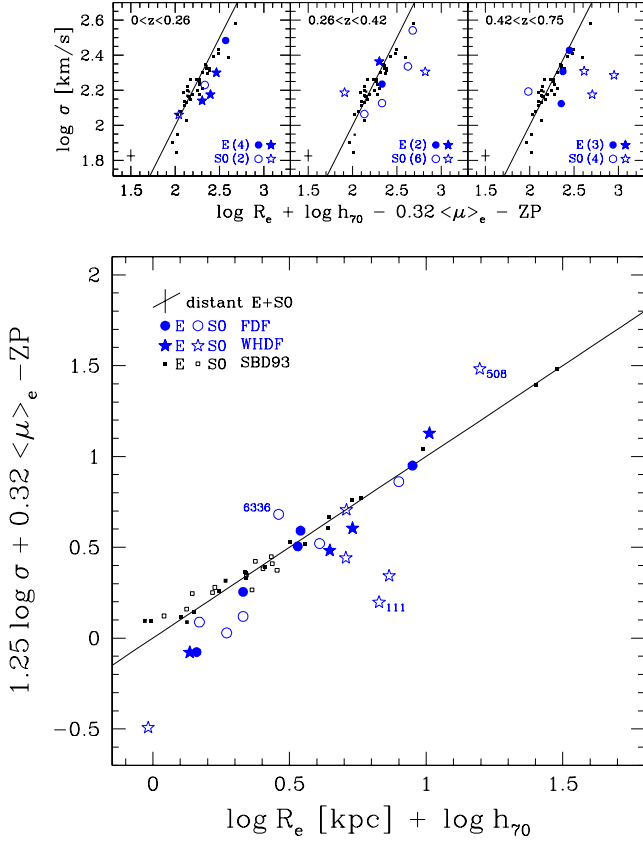
Figure 14. Fundamental Plane for the field early-type galaxies in the FDF and WHDF, compared to the Coma galaxies of SBD93 (small squares) in rest-frame Johnson B-band. Filled symbols denote ellipticals, open symbols S0 galaxies and Sa bulges. *Lower panel:* Edge-on view of the FP. The distant field lenticular galaxies show a stronger evolution and larger scatter than the ellipticals. *Upper panel:* Evolution of the field FP as a function of redshift. Field galaxies are binned into different redshift slices, each compared to the Coma galaxies and shown along the short axis of the edge-on view. Brackets denote the number of galaxies in a respective morphological class (E, S0/Sa). The offset of the distant field galaxies from the local FP increases with redshift, whereas the scatter appears to increase primarily for S0 galaxies with look–back time. Mean error bars are shown in each panel.

The thickness of the FP appears to vary between the individual field galaxy samples. For the FDF an average rms scatter of 0.136 is detected, whereas the WHDF show a larger 1σ dispersion of 0.289. This effect is partly caused by three high redshift objects $0.4 \leq z \leq 0.74$ in the WHDF, which are all disc-dominated galaxies, without these object the rms scatter is 0.202. Dividing the field sample with respect to velocity dispersion at $\log \sigma = 2.275$ or luminosity at $M_B = -21.404$, no strong variations in the amount of evolution between the sub–samples are detected. However, the comparisons rely on the assumed cutoffs in σ and M_B because outliers, such as early Sa spiral galaxies, can strongly influence the derived luminosity evolution. In the next section, possible differences between the stellar populations of elliptical and lenticular galaxies will be addressed.

4.5 Galaxy Types: Ellipticals versus Lenticulars

Looking at differences between the morphological types of *field* early-type galaxies, the S0 galaxies display a stronger evolution than the elliptical galaxies. Assuming that the slope of the local

Table 10. Evolution of the FP in Johnson B-band as derived for the early-type field galaxies in the FDF and WHDF. N shows the number of galaxies and $\Delta \overline{\gamma}$ indicates the mean FP zero-point offset. In the fourth and fifth column, the median FP zero-point evolution $\Delta \langle \gamma \rangle$ and the median evolution in the FP $\Delta \langle \mu_e \rangle$ [in mag] are listed. The last column gives the $\pm 1\sigma$ scatter of the mean offsets.

Sample	N	$\Delta \overline{\gamma}$	$\Delta \langle \gamma \rangle$	$\Delta \langle \mu_e \rangle$	σ_γ
FDF	11	0.066	0.075	-0.235	0.136
WHDF	10	0.199	0.214	-0.667	0.289
FDF+WHDF	21	0.130	0.089	-0.279	0.227
FDF+WHDF[a]	19	0.170	0.126	-0.393	0.197
E	9	0.075	0.075	-0.230	0.121
S0	12	0.171	0.211	-0.643	0.281
S0[a]	10	0.255	0.241	-0.735	0.219
S0[b]	9	0.214	0.211	-0.643	0.185
low lum.[c]	11	0.056	0.082	-0.255	0.180
high lum.	10	0.211	0.165	-0.515	0.254
high lum.[d]	9	0.164	0.126	-0.393	0.219
low mass[e]	11	0.099	0.089	-0.279	0.221
high mass	10	0.163	0.126	-0.393	0.240

[a] Omitting ID 6336 and ID 508, both Sa bulges.
[b] Omitting ID 6336 and ID 508 and ID 111.
[c] lower-luminosity: $M_B > -21.404$, higher-luminosity: $M_B < -21.404$.
[d] Omitting ID 111 at $z = 0.74$.
[e] less-massive: $\log \sigma < 2.275$, more-massive: $\log \sigma > 2.275$.

reference holds valid for the distant galaxies, the 9 field ellipticals show in edge-on projection of the FP a zero-point offset

$$\langle \Delta \gamma_{\rm E}^{\rm f} (z = 0.4) \rangle = 0.08 \pm 0.06, \tag{5}$$

which corresponds to a brightening in their stellar populations of $\Delta M_B^{\rm E} = -0.23 \pm 0.18^m$. By comparison, the nine field lenticulars exhibit an offset in the zero-point with respect to the local Coma galaxies

$$\langle \Delta \gamma_{\rm S0}^{\rm f}(z = 0.4) \rangle = 0.21 \pm 0.09, \tag{6}$$

which corresponds to an average evolution of $\Delta M_B^{\rm S0} = -0.64 \pm 0.27^m$. Note, that this FP offset is very similar if we include the two Sa bulges and results in the same amount of evolution if also the highest redshift lenticular galaxy is accounted for, see Table 10 for details. Errors on the zero-points of elliptical and S0 galaxies were individually derived as

$$\delta {\rm ZP}^2 = \delta {\rm FP}_B^2 + \delta {\rm BS}^2 \tag{7}$$

where $\delta {\rm FP}_B$ denotes the total error which enters the FP in the rest-frame B-band and $\delta {\rm BS}$ is the uncertainty computed through an iterative bootstrap re–sampling of the data points 100 times (Fritz et al. 2005). Limiting the S0 galaxies to redshifts $z < 0.7$ and rejecting the two Sa bulges, the same results are derived (see Table 10). In addition, the field ellipticals obey a tight FP with a small 1σ scatter of 0.121, whereas the S0 types have a larger dispersion of 0.219 (omitting the two Sa bulges). This gives further evidence that the lenticular galaxies have a larger range of different stellar populations.

A faster evolution of the M/L ratios (see next section § 5 and equation 5.1 for a description of the connection between the FP and M/L ratios) of the S0 galaxies with respect to elliptical

galaxies was also found for *cluster* early-type galaxies at $z \sim 0.2$ (Fritz et al. 2005), which are in agreement with a low formation redshift $1 \leq z_{\rm form} \leq 2$. As the slope of the $M/L - M$ relation for these distant cluster galaxies is steeper than those for the Coma cluster galaxies, this can be interpreted as a dependence of the evolution on galaxy mass, and hence a downsizing effect in the evolution of these galaxies.

The evolution of the FP for the early-type FDF and WHDF field galaxies in the rest-frame Johnson B-band is illustrated in Figure 14. Early-type galaxies were binned in redshift space to investigate their location within and along the edge-on FP as a function of redshift and to test the effects of possible outliers. Ellipticals are represented as filled, S0s and Sa bulges as open symbols. For each morphological type the number of galaxies within a redshift bin is indicated in the brackets. Small squares denote the Coma galaxies and the straight line is a principal component fit to the local sample (Ziegler et al. 2005). Figure 14 clearly shows the evolution of the FP for the distant galaxies with respect to the local Coma FP. The offsets of the distant field galaxies increase with redshift but the scatter appears to be mainly amplified for lenticular galaxies. The two galaxies with a "positive" evolution in the last two panels are the Sa bulges ID 6336 and ID 508 and show a clear disc on the ACS images. These objects can mimic on average a weaker evolution in luminosity for the whole galaxy population (cf. Table 10). Regardless of the Sa bulges, the S0s exhibit a larger scatter at higher redshift $0.26 < z < 0.75$ than the ellipticals which suggests that the stellar populations of E and S0 types are different and that lenticulars are a more heterogeneous group. An explanation could be that these S0 galaxies resemble post-starburst galaxies as no strong emission lines were detected in their spectra. This statement will be further addressed in § 5.2.

5   STELLAR POPULATION AGES

5.1   Constraints on the Formation Epoch of Early-Type Galaxies

The observed evolution of the M/L ratio as derived from the FP depends on the age of the stellar population of the galaxies. In general, the luminosity of a young stellar population becomes rapidly fainter when the massive and bright stars which have a short lifetime disappear. For an old population comprising mainly low mass stars the dimming of the luminosity proceeds on a more gradual evolutionary path. As a consequence of this, a stellar population formed at lower redshift will evolve faster than one generated at high redshift. In the following, the observed evolution of the M/L ratio will be compared to simple stellar population models of a single burst formed at redshift $z_{\rm form}$. The models have been generated following the description of the analytic models by van Dokkum & Franx (2001b).

The luminosity evolution of a single-age stellar population can be described by a power law as

$$L \propto \frac{1}{(t - t_{\rm form})^\kappa}, \tag{8}$$

where $t_{\rm form}$ is the stellar formation time which corresponds to a formation redshift of $z_{\rm form}$ (e.g., Tinsley 1980). The coefficient κ depends on the IMF, the metallicity and the chosen passband in which the luminosity is measured. In the stellar population models by Bruzual & Charlot (2003), a normal IMF with Salpeter (1955) slope, solar metallicity and $\kappa_B = 0.96$ for the rest-frame B-band was adopted. Model predictions are shown in Figures 15 to 16 for

the field elliptical and S0 galaxies in the rest-frame B-band. Note that the predicted evolution of the models is independent of H_0 as the age dependence of the M/L ratio is a power law. Two different model tracks for a single stellar population with formation redshift $z_{\rm form} = 1$ (lower line) and $z_{\rm form} = 2$ (upper line) are indicated as the dotted lines in Figures 15 to 16.

To assess the evolution of the stellar populations in the early-type galaxies, the evolution of the FP zero-point γ for the distant galaxies can be directly converted into an evolution of the average M/L ratio as

$$\langle \Delta \log(M/L) \rangle = -\frac{\langle \Delta \gamma \rangle}{2.5\beta}, \tag{9}$$

where the average evolution of $\Delta \log(M/L)$ was derived via the average zero-point offset of the distant FP $\langle \Delta \gamma \rangle$ from the local Coma FP (Treu et al. 2001).

In a recent study of 27 field early-type galaxies between $0.6 < z < 1.15$ a mass-dependent evolution was found (van der Wel et al. 2005). This sample of high-redshift galaxies showed that the evolution of low-mass field galaxies with a characteristic mass of $M < 2 \times 10^{11} M_\odot$ is faster than their more massive counterparts. Similar results have been drawn from field early-type galaxies at $z \sim 1$ from the GOODS-N sky region (Treu et al. 2005) and from the K20 survey (di Serego Alighieri et al. 2005). The 21 field early-type galaxies in our sample are located at a lower redshift range of $0.2 < z < 0.75$. But it is very interesting, if already at a look-back time of ~ 5 Gyr a possible evidence for a mass-dependent evolution or at least a trend with galaxy mass can be detected. For this reason, the average evolution of the M/L ratio of the field elliptical and S0 galaxies in the FDF and WHDF was derived.

Figure 15 displays the average evolution of the M/L ratios for the field galaxies in the rest-frame B-band compared to the early-type cluster galaxies taken from van Dokkum & Stanford (2003). For a compilation of massive early-type galaxies with $M > 2 \times 10^{11} M_\odot$ in rich clusters of galaxies taken from the literature these authors deduced an average formation redshift of $z_{\rm form} \approx 3$, which is indicated as the solid line. All calculated model tracks are forced to go through the average M/L ratio of the field galaxies at $z = 0.02$ by Faber et al. (1989), shown as the small dot in Figures 15 and 16. The field FDF and WHDF sample was splitted according to the characteristic mass at $M = 2 \times 10^{11} M_\odot$, which gives 13 lower-mass and 8 higher-mass galaxies. The average evolution of the higher-mass field galaxies is $\langle \Delta \ln(M/L_B) \rangle = -0.31 \pm 0.06$ at a redshift of $\langle z \rangle = 0.44$. Lower-mass galaxies indicate on average a stronger evolution of $\langle \Delta \ln(M/L_B) \rangle = -0.54 \pm 0.07$ at $\langle z \rangle = 0.38$. The slight deviation in the redshift is solely due to the not uniform number of galaxies in each sub-sample. Massive field galaxies are in compliance with a slow evolution as derived for the massive cluster galaxies and a high formation redshift for the bulk of the stars of $z_{\rm form} \approx 3$. In contrast, less-massive field galaxies in the FDF and WHDF with $M < 2 \times 10^{11} M_\odot$ evolve faster and follow an evolutionary track between $1 \lesssim z_{\rm form} \lesssim 2$ which is similar to the less-massive cluster galaxies from van Dokkum & Stanford (2003), which is indicated as the open square in Figure 15. This result gives evidence that already at a look-back time of ~ 5 Gyr differences in the measured M/L evolution for the FDF and WHDF field galaxies can be revealed.

To translate the evolution in the M/L ratios into a specific formation redshift $z_{\rm form}$ for the field galaxies, the evolution of the M/L ratios for the individual field early-type galaxies are investigated. Figure 16 illustrates the offset from the local FP in the rest-
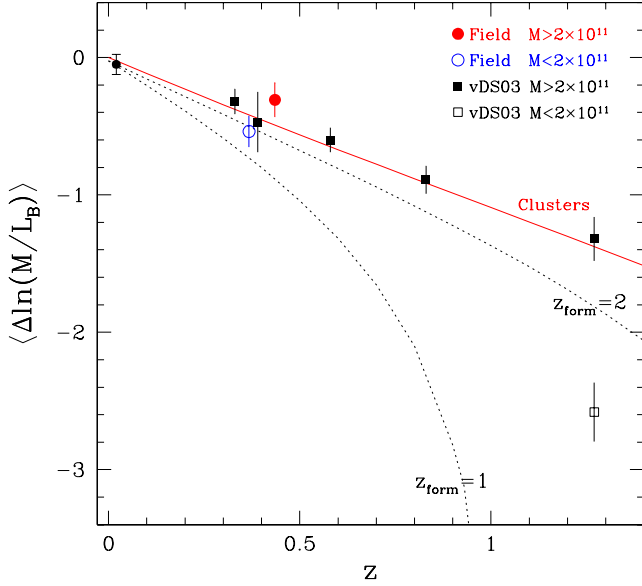
Figure 15. The average evolution of the M/L ratio of the *field* elliptical and S0 galaxies in the FDF and WHDF and the cluster early–type galaxies taken from van Dokkum & Stanford (2003), in the rest–frame B-band. Dotted lines are model tracks for a single stellar population with formation redshift 1 (lower line) and 2 (upper line). The model tracks are forced to go through the small dot which represents the average M/L ratio of the field galaxies at $z = 0.02$ by Faber et al. (1989). The solid line is the best fitting formation redshift for the evolution of massive cluster galaxies with masses $M > 2 \times 10^{11} M_\odot$. Massive field galaxies with $M > 2 \times 10^{11} M_\odot$ show a similar slow evolution as cluster galaxies, whereas less–massive field galaxies with $M < 2 \times 10^{11} M_\odot$ evolve faster, similar to less–massive cluster galaxies.

Figure 16. The evolution of the M/L ratio of the *field* elliptical and S0 galaxies in the FDF and WHDF and the field early-type galaxies at $\langle z \rangle = 1$ taken from van der Wel et al. (2005), in the rest–frame B-band. Dotted lines are model tracks for a single stellar population with formation redshift 1 (lower line) and 2 (upper line). The model tracks are forced to go through the small dot which represents the average M/L ratio of the field galaxies at $z = 0.02$ by Faber et al. (1989). The solid line is the best fitting formation redshift for the evolution of cluster galaxies with masses $M > 2 \times 10^{11} M_\odot$. The scatter in the M/L ratios is large but there is a clear trend for field S0 galaxies to evolve faster. Field ellipticals appear to form two separate groups with respect to M/L ratios.

frame B-band for elliptical and S0 galaxies in the FDF and WHDF. A comparison sample of 27 field early-type galaxies, splitted into less-massive $M < 2 \times 10^{11} M_\odot$ (blue, open symbols) and more-massive field galaxies $M > 2 \times 10^{11} M_\odot$ (red, filled symbols), at high redshift $0.6 < z < 1.15$ by van der Wel et al. (2005) is also shown. Again, model tracks for a single-age stellar population with formation redshift 1 (lower line) and 2 (upper line) are displayed as dotted lines. All model tracks were normalised to the average M/L ratio of the field galaxies at $z = 0.02$ by Faber et al. (1989), indicated as the small black dot. The evolution of cluster galaxies with masses $M > 2 \times 10^{11} M_\odot$ can be best approximated assuming a formation redshift of $z_{\rm form} \approx 3$, which is denoted as the solid line in Figure 16. For our field early-type galaxies we measure an evolution of $\Delta \ln(M/L_B) = -(1.71 \pm 0.18) z$. Although the scatter in the offsets from the local FP is large, a clear trend for a faster evolution of field S0 galaxies is found. On the other hand, field elliptical galaxies appear to form two separate groups with respect to M/L ratios. To assess the formation redshift $z_{\rm form}$, we split our field galaxy sample into a low- and high-mass sample at $M = 2 \times 10^{11} M_\odot$. An unrestricted linear χ^2-fit to the low-mass early-type field galaxies with $M < 2 \times 10^{11} M_\odot$ gives

$$\Delta \ln(M/L_B) = -(1.25 \pm 0.56) z - (0.08 \pm 0.41). \qquad (10)$$

This would correspond to a formation redshift of $z_{\rm form} = 1.9 \pm 0.5$. The error on $z_{\rm form}$ denotes the observed (1σ) scatter in the $\Delta \ln(M/L_B) - z$ relation. For the higher-mass galaxies with $M > 2 \times 10^{11} M_\odot$ a linear χ^2-fit yields

$$\Delta \ln(M/L_B) = -(0.89 \pm 0.75) z - (0.02 \pm 0.25). \qquad (11)$$

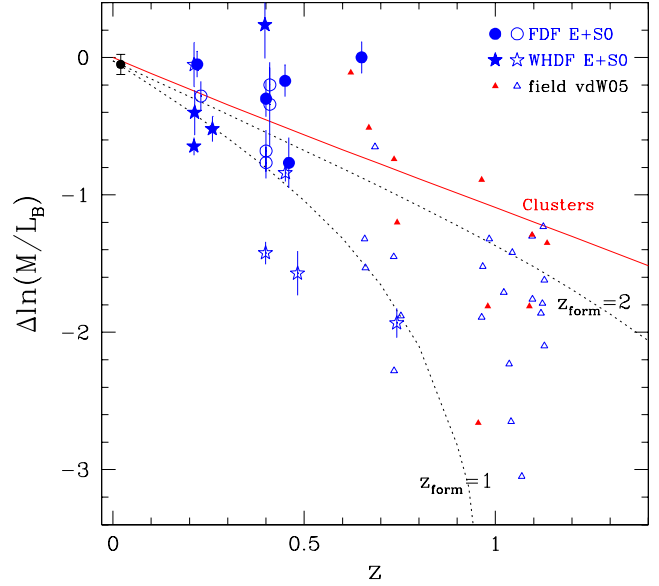For the massive early-type field galaxies, the evolution of the M/L

predicts a mean star formation epoch for the bulk of their stellar populations of $z_{\rm form} = 3.5 \pm 1.3$. In comparison to the lower-mass counterparts, a higher formation redshift is significant on the 2σ level based on the uncertainty of the high-mass galaxies. The lack of field galaxies with masses of $M > 2 \times 10^{11} M_\odot$ introduces a larger uncertainty on the $z_{\rm form}$ value. By comparing the derived formation epoch of the high–mass cluster galaxies with numbers for cluster galaxies in the literature a good agreement is found. Based on a compilation of clusters out to redshift of $z = 1.27$, van Dokkum & Stanford (2003) deduce $z_{\rm form} = 2.6^{+0.9}_{-0.4}$. This study gives an upper limit for the formation redshift of massive cluster galaxies of $z_{\rm form} = 3.5$ (1σ). The result obtained for the massive field galaxies here is within this upper limit, which suggests that these field galaxies have old passively evolving stellar populations similar to their massive counterparts in clusters. Besides the scatter of the individual galaxies, lower-mass field galaxies have a stronger evolution in their M/L ratio. The mean stellar population ages of the less-massive field galaxies are younger, with lower formation redshift of $1 < z_{\rm form} \leq 2$. This suggests a *mass–dependent luminosity evolution* with a stronger evolution for lower–mass galaxies with $M < 2 \times 10^{11} M_\odot$.

The rest-frame optical colours offer a powerful tool to investigate the origin of the scatter in $\Delta \ln(M/L_B)$. Figure 17 displays the M/L ratios as a function of the rest-frame $(B - I)$ colour for our early-type field galaxies. As expected from stellar population model predictions, galaxies with lower M/L ratios should have bluer colors than galaxies with higher M/L. Indeed, lower-mass galaxies (with low M/L ratios) are on average bluer than higher-mass galaxies (with high M/L ratios). Galaxies with low M/L
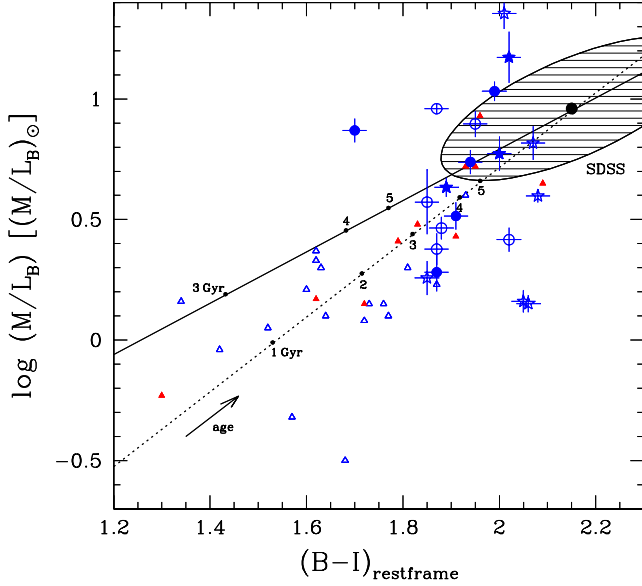
Figure 17. M/L_B as a function of the rest-frame $(B-I)$ colour for early-type field galaxies in the FDF and WHDF. Symbol notations as in Figure 16. The median scatter in the M/L_B and $(B-I)$ colour distribution of massive field early-type galaxies ($M > 2 \times 10^{11}$) in the SDSS is indicated by the shaded ellipse. For comparison, two different Bruzual & Charlot model predictions with solar metallicity are shown, for a single stellar population (dotted line) and for an exponentially declining star formation with $\tau = 1$ Gyr (solid line). Both model tracks are forced to match the local values as defined by the SDSS comparison sample.
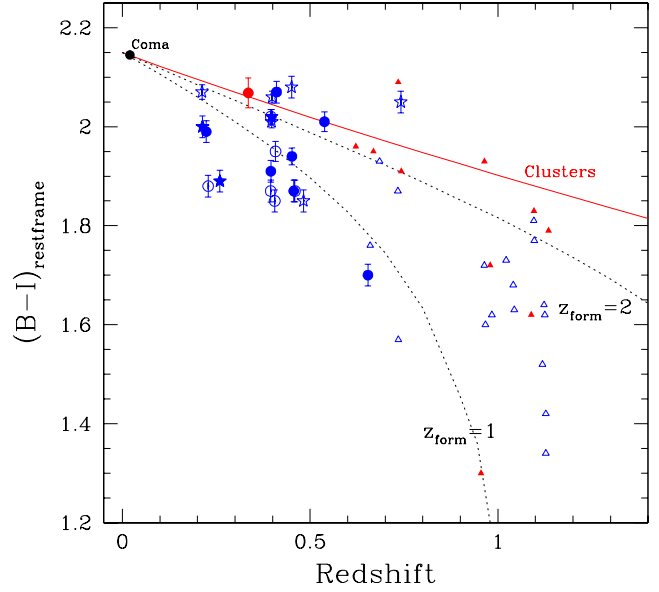

Figure 18. Evolution of the rest-frame $(B-I)$ colour with redshift for early-type field galaxies in the FDF and WHDF. Symbol notations as in Figure 16. The solid (red) point shows the median $(B-I)$ colour of early-type cluster galaxies in the FDF.

ratios follow the predictions of a single stellar population with solar metallicity by Bruzual & Charlot (2003), indicated as the dotted line in Figure 17 and form an extension to the higher redshift sample by van der Wel et al. (2005). Field galaxies with higher M/L ratios populate a transition zone to the color and M/L ratios regime as defined by the local SDSS sample.

In Figure 18 the rest-frame $(B-I)$ colour as a function of redshift is displayed for our early-type field galaxies. As a comparison, we also indicate the median $(B-I)$ colour derived for early-type cluster galaxies in the FDF (see also § 2.3.3). If we compare the Figures 16 and 18, strong similarities can be found. The strong correlation between M/L and galaxy colour and a similar evolution in M/L and in colour indicates that the observed evolution and scatter in M/L are intrinsic to the galaxies and due to differences in their stellar populations. Note, that in this Figure also galaxies for which no M/L ratios could be derived are shown. If the sample is equally split according to the characteristic mass separation as introduced in Figure 15, lower-mass galaxies with $M < 10^{11} M_\odot$ have on average bluer colours (median colour of $\langle (B-I) \rangle = 1.88$ than more-massive galaxies with $M > 10^{11} M_\odot$ which feature redder colours of $\langle (B-I) \rangle = 2.00$.

To test the detected mass–dependent evolution even further, Figure 19 displays the M/L_B ratio of the early-type field galaxies as a function of mass M. The galaxies were divided according to their redshift into two different bins. The left panel shows the $M/L_B - M$ for all field galaxies, whereas in the right panel the field objects are restricted to a sub-sample of 14 high-redshift galaxies. As a comparison, the nearby Coma cluster sample (small dots) and the high-redshift field E+S0 galaxies at $z \sim 1$ of van der Wel et al. (2005) (triangles) are indicated together with linear χ^2-fits to both samples. All data points have been corrected

for maximum progenitor bias $\Delta \ln(M/L_B) \approx 0.2\, z$. Ellipticals, in particular below $z \lesssim 0.26$, follow the local relation whereas the S0 galaxies have on average lower M/L ratios and match the intermediate–mass range of the $z \sim 1$ field E+S0 galaxies. Lenticular galaxies show a larger scatter and the two outliers in the FP represent the two Sa bulges (ID 6336 and ID 508) that are clearly offset from the rest of the sample. The difference between field elliptical and S0 galaxies found in the FP can be explained by a difference in their formation epochs. Ellipticals, especially massive ones, were generated at earlier times and follow rather moderate quiescent evolutionary tracks. On the contrary, lenticular and Sa bulges show more diverse stellar populations which are younger and have been formed at recent times with formation redshifts $1 < z_{\rm form} \leq 2$.

5.2   Independent Diagnostics of Star Formation

In Figure 17 we have shown that the mass-to-light ratio correlates well with the rest-frame $B - I$ color. As independent diagnostic tools for star formation, we also compare the equivalent widths of [O II] and Hδ_A to stellar population models.

Using the [O II] and Hδ_A star formation indicators (see § 2.3.4) allows us to probe different time scales of star formation episodes in our sample galaxies. Assuming a passive evolution, for systems with old stellar populations (average age of >1 Gyr) with no emission lines in their spectra, the equivalent widths of Balmer absorption lines decrease continuously over time. Within the first $\sim 10^8$ yr of the generation of new stars in these galaxies the equivalent width of Hδ increases rapidly up to its maximum value around 10Å. Afterwards the Balmer line decreases steadily until the stellar population reaches an age of 2 Gyr. This can be interpreted that substantial star formation events ($\sim 30\ M_\odot\ {\rm yr}^{-1}$) occurred in the first $\sim 10^8$ yr of the systems with subsequent weak star formation thereafter. In case of the [O II] emission line, it offers an diagnostic that is sensitive to ongoing or very recent star formation episodes ($\lesssim 50$ Myr).

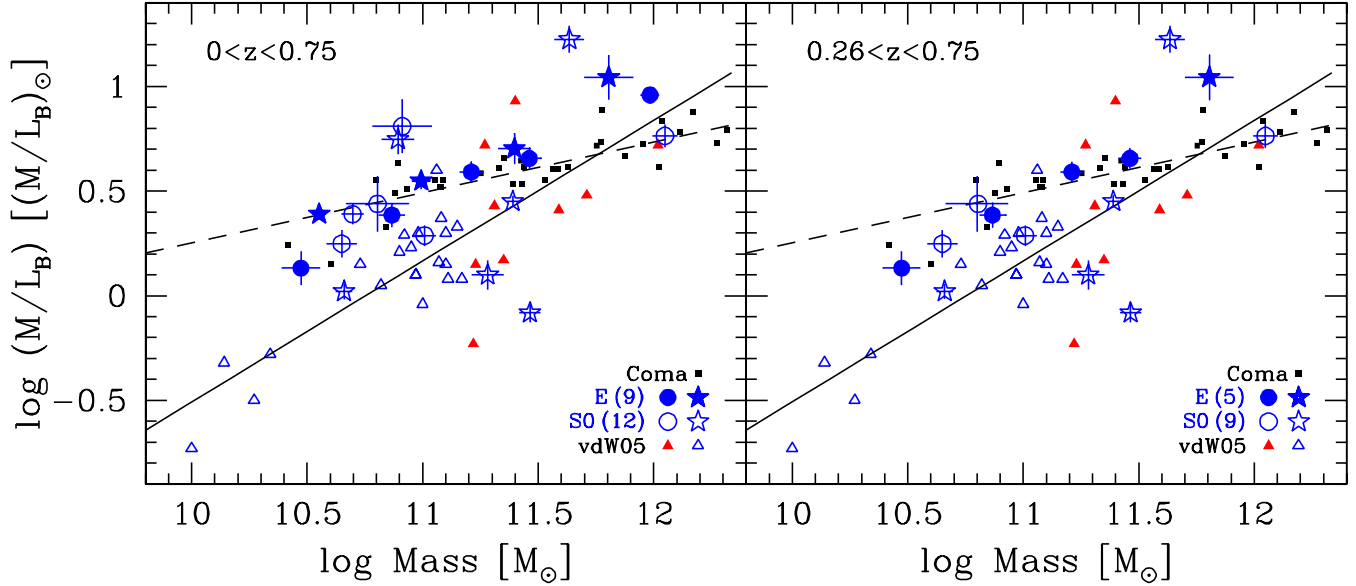The evolution of the Hδ_A absorption line strength with red-

Figure 19. M/L_B ratio as a function of mass M in solar units as derived from the FP for the early-type field galaxies in the FDF and WHDF, divided into two different redshift bins. Filled symbols denote ellipticals, open symbols S0 galaxies and Sa bulges. In brackets the respective number of a morphological class is listed. Errors for the distant sample are shown in both panels. The nearby Coma cluster sample is indicated with small dots (dashed line is a χ^2-fit to Coma) and the high-redshift field E+S0 galaxies at $z \sim 1$ by van der Wel et al. (2005) are shown as triangles (solid line is a χ^2-fit). All data points have been corrected for maximum progenitor bias $\Delta \ln(M/L_B) \approx 0.2\,z$. *Left:* $M/L_B - M$ for the whole sample of 21 field E+S0 galaxies $0 < z < 0.75$. *Right:* $M/L_B - M$ for 14 higher-redshift field E+S0s with $0.26 < z < 0.75$. Ellipticals follow the local relation whereas the S0 galaxies have on average lower M/L ratios, a larger scatter and match the intermediate–mass range of the $M/L_B - M$ relation of the $z \sim 1$ field E+S0 galaxies.

shift of our field galaxies is presented in Figure 20. We compare our $H\delta_A$ measurements to the $H\delta_A$ determinations of field galaxies up to $z \sim 1$ by Treu et al. (2005) and galaxies with strong $H\delta$ absorption in the Gemini Deep Deep Survey (GDDS) by Le Borgne et al. (2006). For consistency with previous studies we define systems with $H\delta_A > 4$ Å as being galaxies with strong $H\delta$ absorption. Two sets of different stellar population models by Bruzual & Charlot (2003) are also indicated. Compared to the $H\delta$-strong galaxies, the field galaxies in the WHDF and FDF exhibit lower $H\delta_A$ absorption features. Non of our systems exhibit very strong $H\delta_A$ equivalent width, in particular all galaxies gave $H\delta_A \leq 2.60 \pm 0.23$ Å. Therefore, they are most likely not systems with strong $H\delta$ absorption. They follow the evolution track of the composite stellar evolution model consisting of an initial burst of SF at $z_{f1} > 2$ and a secondary SF burst at $z_{f2} < 1.2$. A single stellar population model consisting of a main star burst forming 90% of the total stellar content at $z_f = 5$ is consistent with three galaxies. All these galaxies show both stronger $H\delta_A$ absorption and additional [O II] 3727 emission in their spectra and have experienced a very recent episode of star formation (see next section 5.2.1 for further details).

5.2.1 Recent Star Formation

Six galaxies in our sample feature [O II] 3727 emission lines in their spectra. Two of these are spiral bulges (ID 158 and ID 508), three are of intermediate type S0/Sa (ID 946) and E/S0 (ID 111 and ID 173) and one is an elliptical galaxy (ID 437). For these objects, the main questions of interest are the star formation rate (SFR), the mass fraction involved in the star formation and the duration of the star formation episode.

In oder to convert the [O II] 3727 equivalent width to star formation rates, we assume that the equivalent width measured within the aperture is a representative diagnostic for the global value of the

galaxy. The observed luminosity $L([O\,II])_{obs}$ of the [O II] emission line can be derived as:

$$L([O\,II])_{obs} = (1.4 \pm 0.3) \times 10^{29} \frac{L_B}{L_{B,\odot}} \text{EW}([O\,II]) \, [\text{ergs s}^{-1}], \quad (12)$$

with $L_B/L_{B,\odot} = 10^{0.4\,(M_{B,\odot} - M_B)}$ and $M_{B,\odot} = 5.48$ (Kennicutt 1992; Balogh et al. 1997). The observed (measured) $L([O\,II])_{obs}$ is related to the intrinsic $L([O\,II])_{int}$ luminosity as

$$L([O\,II])_{int} = 3.11 \times 10^{-20} \, L([O\,II])_{obs}^{1.495}. \quad (13)$$

Equation 13 takes into account the intrinsic reddening. To derive the total SFR in units of solar masses per year, we use the relation established by Kewley et al. (2004):

$$\text{SFR} = 6.58 \times 10^{-42} \, L([O\,II])_{int} \, [M_\odot \, \text{yr}^{-1}]. \quad (14)$$

Since we do not know the oxygen abundances of our galaxies, we have chosen to adopt the average calibration by Kewley et al.

Using our observed [O II] equivalent widths, we derive for the six emission-line galaxies a median SFR of 6.2 $M_\odot \, \text{yr}^{-1}$. For the four E+S0 galaxies we find a median SFR of 3.7 $M_\odot \, \text{yr}^{-1}$, whereas the SFR for two Sa bulges is 15.5 $M_\odot \, \text{yr}^{-1}$. Instead, transforming our observed [O II] equivalent widths to rest-frame and assuming the relationship reported by Balogh et al. (1997) with a global extinction correction of E(Hα)=1 mag, we find for the whole sample a median SFR of 2.5 $M_\odot \, \text{yr}^{-1}$. The SFRs for the E+S0 and Sa galaxies are 2.5 and 9.1 $M_\odot \, \text{yr}^{-1}$, respectively. If we correct the absolute B-band magnitude of our galaxies using the luminosity difference of the distant galaxies and the low-redshift reference sample as derived from the FP, we get a mean mass of these galaxies of $1.48 \times 10^{11} \, M_\odot$ (median $1.98 \times 10^{11} \, M_\odot$). Assuming an 1 Gyr burst of star formation with the mean SFR found for the [O II] line would have involved between 3% to 10% (median about 5%) of the stellar mass of the field galaxies. We would expect that the in-
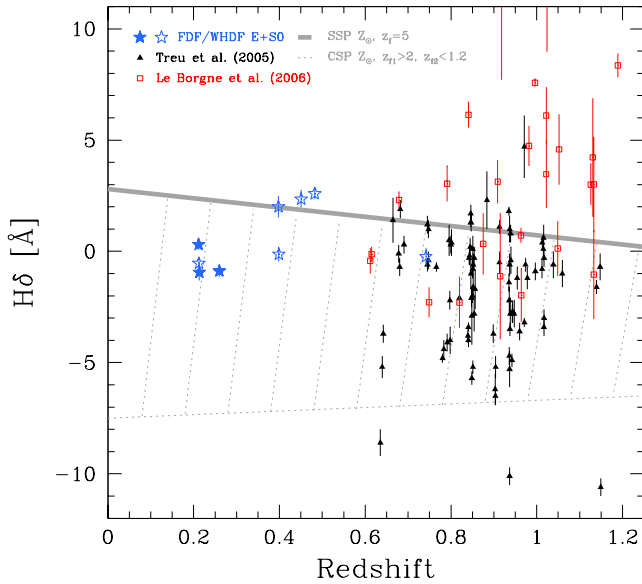
Figure 20. Evolution of the Hδ_A line strength as a function of redshift for a set of two-burst stellar population models consisting of a main star burst forming 90% of the total stellar mass at $z_f = 5$, plus a secondary burst forming 10% of the stellar mass at $z_{f2} < z_{f1}$ with $z_{f2} < 1.2$ (models from Bruzual & Charlot 2003). Hδ_A measurements for our field E+S0 galaxies are denoted by the large symbols, the Hδ_A measurements by Treu et al. (2005) and Hδ-strong galaxies in the GDDS by Le Borgne et al. (2006) are shown as the triangles and open squares, respectively.

volved mass in the SF burst should appear to be strongly dependent on the galaxy mass. However, our sample statistics of galaxies with recent SF are too small and the galaxies are spread among different redshifts to give further constraints.

To further constrain the duration and the mass fraction involved in the star formation episode we compared our measurements to sets of 'toy' models that consist a mix of two stellar populations (Bruzual & Charlot 2003). Line emission are either caused by a small mass fraction (3%) involved in the star formation burst suggesting $z_{form} = 1.1$, or if a larger mass fraction (10%) is adopted the episode should have been started earlier $z_{form} = 1.7$.

In general, line emission is evidence for star formation activity or an AGN which increases the average luminosity of the galaxy and thereby causing the system to be offset from the local FP relation. In contrast to what is expected, the galaxies with detected ongoing SF in our sample indicate no offset along the edge-on projection of the FP but a tight relation. Based on our measurements we estimate that the stellar mass fraction involved in the SF episode must be in order of 25% to result in a visible effect within the FP. The emission-line galaxies in our sample indicate no signs of interactions or merging events that could trigger the star formation episodes in these objects. We therefore find no evidence for a connection between star formation activity and interaction signatures or mergers.

6   COMPARISON WITH PREVIOUS RESULTS

Over the past few years, several groups have measured the M/L evolution of field early–type galaxies at different redshifts, either using direct mass measurements that involve the internal stellar kinematics of the galaxies (Treu et al. 2001, 2002; van Dokkum et al. 2001a; van Dokkum & Ellis 2003;

Gebhardt et al. 2003; van der Wel et al. 2005; Treu et al. 2005) or modelling the stellar kinematic structure and mass profile from the separation of multiple gravitationally lensed images of background galaxies (van de Ven et al. 2003; Rusin & Kochanek 2005). In the following we will compare these previous results in the literature with our findings, and comment on possible inconsistencies that exist between the datasets. Table 11 gives a compilation of the M/L evolution as reported by various groups based on different datasets. For comparison, we also list the methods and selection criteria of each of the studies, where T corresponds to a selection based on morphologies. In the methods we present the two most popular techniques in measuring the internal kinematics of E+S0 galaxies, either using the stellar velocity dispersion $\sigma_\star$ or using separation of gravitational lensed images via an isothermal model ('lensing isothermal') or more complex algorithms ('lensing complex'). Besides the magnitude limited samples, there are two studies that analysed the same sample of lensing galaxies (van de Ven et al. 2003; Rusin & Kochanek 2005). The predictions based on lensing properties of early-type galaxies agree with one another to within their quoted uncertainties. Most of these studies report that early-type lens galaxies appear to have nearly isothermal mass density profiles (e.g., van de Ven et al. 2003). Rusin & Kochanek (2005) took a different approach and described the mass distribution using statistical model assumptions where the galaxy populations are described by a range of star formation redshifts allowing for a scatter created by deviations from homology or spread in formation epochs. Both methods of lensing and direct mass measurements agree quite well within their uncertainties, although lensing appears to predict a slightly slower M/L evolution of the galaxies. From comparison with other results, we found that differences in the fitting technique can change the amount of evolution in $\ln(M/L_B)/z$ for each data sample by up to 26%.

Using direct kinematic measurements, two groups have drawn samples of field galaxies from the CDFS to study their evolution at $0.6 \lesssim z < 1$ (van der Wel et al. 2005; di Serego Alighieri et al. 2005). However, these different teams found rather inconsistent galaxy sizes and velocity dispersions for both individual and same objects. Discrepancies arise most likely because these studies used different fitting algorithms for both galaxy parameters (sizes and kinematics). di Serego Alighieri et al. (2005) argue that their smaller sizes are due to a selection effect of compact galaxies. These objects are rather faint and have low velocity dispersions (1/3 of the galaxies have $\sigma < 100$ km s^{-1}) and thus could be either biased to early-type spirals or low-luminosity early-type galaxies containing faint discs that are unresolved. This argument gets support by their small measured Sérsic indices. In addition, the large spectroscopic apertures used in their work may cause to underestimate a substantial rotational support in the case of faint low-luminosity galaxies. The most likely explanation between the differences of di Serego Alighieri et al. (2005) and van der Wel et al. (2005) might be the selection of the target objects and the different analysis tools, where the former primarily selected fainter galaxies whereas the latter included also higher-luminosity (hence more-massive) galaxies.

Additional selection effects may arise from small number statistics, noise introduced by cosmic variance or the use of shallow imaging data which results in a contamination by bulge-dominated spiral galaxies. Further, low-S/N spectra cannot disentangle galaxies with post-starburst spectra (i.e., Hδ-strong galaxies) from spectra of normal passive galaxies. Unfortunately our current analysis is limited with respect to the sample size. However, effects due to imperfections of data quality can completely be ruled out in case

Table 11. Compilation of previous results on field galaxies

Reference	$\Delta \ln (M/L_B)/z$ reported	$\Delta \ln (M/L_B)/z$ high mass	$\Delta \ln (M/L_B)/z$ low mass	$\langle \log(M/M_\odot) \rangle$	$\langle z \rangle$	N	Method; Selection
(1)	(2)	(3)	(4)	(5)	(6)	(7)	(8)
Treu et al. (2001)	-1.64 ± 0.12	-1.55 ± 0.27	-1.47 ± 1.89	2.3×10^{11}	0.29	19	$\sigma_\star$; T, magnitude, colour
van Dokkum et al. (2001)	-1.35 ± 0.35	-1.29 ± 0.39	-1.94 ± 0.33	1.5×10^{11}	0.42	18	$\sigma_\star$; T, magnitude
Treu et al. (2001, 2002)	-1.66 ± 0.37	$\cdots$	$\cdots$	2.5×10^{11}	0.38	29	$\sigma_\star$; T, magnitude, colour
van Dokkum & Ellis (2003)	-1.25 ± 0.25	-1.41 ± 0.29	-1.77 ± 0.24	1.3×10^{11}	0.56	27	$\sigma_\star$; T, magnitude
Gebhardt et al. (2003)	-1.84 to -2.21	-1.59 ± 0.49	-2.05 ± 0.17	8.5×10^{10}	0.64	21	$\sigma_\star$; magnitude, absorption lines
van de Ven et al. (2003)	-1.43 ± 0.30	-1.13 ± 0.31	-1.71 ± 0.30	2.3×10^{11}	0.54	21	lensing isothermal, lenses
Rusin & Kochanek (2005)	-1.15 ± 0.44	$\cdots$	$\cdots$	$\cdots$	0.54	21	lensing complex; lenses
van der Wel et al. (2005)	-1.75 ± 0.16	-1.20 ± 0.18	-1.97 ± 0.16	1.6×10^{11}	0.90	27	$\sigma_\star$; T, magnitude
Treu et al. (2005)	-1.66 ± 0.11	$\cdots$	$\cdots$	1.3×10^{11}	0.56	141	$\sigma_\star$; T, magnitude
This work	-1.71 ± 0.18	-0.89 ± 0.19	-1.25 ± 0.30	1.0×10^{11}	0.40	24	$\sigma_\star$; T, magnitude, colour

Column 2 gives the values of the evolution of the M/L ratios as reported in the listed studies. Column 3 shows the evolution of galaxies more massive than $M = 2 \times 10^{11} M_\odot$, and column 4 lists the evolution of less massive galaxies. In columns 5 to 7, average masses, redshifts, and sample sizes (N) of the data sets are given. The last column shows the method of deriving the velocity dispersion, '$\sigma_\star$' using stellar kinematics , 'lensing isothermal' σ estimate from image separation using an isothermal model and 'lensing complex' uses a more complex model including statistical variations. When two references are given, the results are based on data of both studies. The reported values are all uncorrected for selection effects. Gebhardt et al. (2003) do not give an error and the average evolution corresponds to $0.8 < z < 1.0$.

of our investigation, as our sample is based on deep imaging photometry and high S/N galaxy spectra. Apart form the work of Gebhardt et al. (2003), our study comprises the field sample with the lowest average masses of galaxies. Therefore, the lower-mass range where effects of differences in the evolution should be more pronounced can be investigated in greater detail. In the nearby future, we will address both important restrictions of number statistics and cosmic variance that impact high redshift studies (A. Fritz et al. 2009a, in preparation).

7 DISCUSSION AND IMPLICATIONS

7.1 AGNs

Some previous studies have investigated the possible influence of the nuclear activity on the evolution of early-type galaxies. Woo et al. (2004, 2005) find no differences in the evolution of the FP for BL Lac objects and radio galaxies with a central AGN from normal early-type galaxies up to $z \sim 0.5$. However, their sample consists of high-luminosity galaxies, hence it is biased towards high-mass galaxies, in particular $M > 3 \times 10^{11} M_\odot$. van der Wel et al. (2005) detected in an FP analysis of field early-type galaxies up to $z \sim 1$ that 4 out of 11 galaxies at $z < 0.8$ (36%) and one out of 16 for $z > 0.9$ show AGN activity. Although their galaxies with AGN are twice as massive than galaxies without AGN they show similar M/L evolution and (no blue) rest-frame $(B - I)$ colours. The authors suggest that the difference between AGN and non-AGN galaxies may become more apparent at higher redshift $z > 0.8$. A similarly low number of AGN galaxies was detected within the sample of Treu et al. (2005), who identified out of 26 E+S0 X-ray counterparts nine AGN based on X-ray luminosity (XAGN), 16 LLAGN (see section 3.5 and Appendix § B for these group definitions), but only two out of 13 [O II] -emitting E+S0 galaxies as secure AGN. The total early-type galaxy sample of Treu et al. (2005) has a quite low contribution of AGN activity (16%) and none of the spectra shows signs of significant SFR, with an upper limit of $\sim 30~M_\odot$ yr^{-1}.

We find three candidates in our field galaxy sample ($\leq 13\%$) that show weak evidence for hosting an AGN (see section 3.5). Our observations suggest a very mild evolution in the absolute numbers of AGN hosts up to $z \approx 0.7$. This is consistent with the results of the stellar mass function of AEGIS field galaxies Bundy et al. (2008), where the abundance of X-ray selected AGN host galaxies ($L > 10^{42}$ ergs s^{-1}) decreases roughly by a factor of two from $z \approx 1.2$ to $z \approx 0.5$, but remains relatively flat across the stellar mass range of $10.35 < \log(M/M_\odot) < 11.70$. However, possible contributions due to LLAGN and/or emission from soft extended X-ray halos or LMXBs could have influence on the activity of our individual galaxies as well. For our field galaxies we measure an average contribution of LMXBs to the X-ray emission in the K-band of L_X(LMXB)$\leq 18\% \pm 6\%$. The X-ray luminosities in our distant galaxies show a weak excess in the soft diffuse X-ray plasma emission, depending on the established local $L_X - L_B$ relationship, between $\leq 7\% \pm 3\%$ to $\leq 26\% \pm 15\%$ compared to the local reference. The increased luminosities are most likely originating from a net effect of star formation and/or LLAGN. A more detailed discussion of these findings and their implications can be found in the Appendix § B.

Blue (central) cores in galaxies are not a stringent indicator for a central AGN power source. For example, within the field early-type galaxy sample of Treu et al. (2005) only 8% show signs of central blue rest-frame colours with $\delta(B - V) \geq 0.2$, and only two of these objects (1%) appear also to host an AGN based on their high X-ray luminosity ($> 10^{42}$ ergs s^{-1}). This suggests that the colour information of the galaxies is not a very powerful technique to distinguish active from non-active galaxies. As there is no multi-band HST photometry for our sky fields available, we thus cannot investigate the colour gradients in our E+S0 galaxies.

7.2 Signatures of Star Formation Quenching

To establish and explore the evolutionary link between E+S0 galaxies at high redshift and their local descendants, we assume that E+S0 galaxies comprising passive (red and "dead", non-

starforming) old stellar populations at high redshift will only be subject to a pure passive evolution in luminosity through $z = 0$. Our approach is justified by the colour evolution of galaxies populating the red sequence following a pure passive evolution (Bell et al. 2004; Faber et al. 2007). In the next step, we adopt the luminosity dimming as derived from the evolution of the FP (see § 5) as $\Delta \ln(M/L_B) = -(1.71 \pm 0.18) z$ and correct for progenitor bias. This latter effect also compensates for a possible (morphological) transformation of galaxies which end up as being classified as passive local E+S0 galaxies. Massive field E+S0 galaxies show a smaller offset from the M/L-relation, whereas less massive ones evolve faster which is supported by younger stellar populations (see section 5.1). Independent of the luminosity of our galaxies, we apply this relationship to all galaxies in our sample and then investigate a possible dependence of the evolution on luminosity and the physical mechanisms that drive our measured mass dependent evolution. The luminosity of the distant E+S0 galaxies is then decreased by a rate of $\Delta \log L_B = 0.74 z$ to obtain their absolute (rest-frame) B-band magnitude at $z = 0$ as

$$M_B(z=0) = M_B(z) + (0.78 \times 2.5 \times z) = M_B(z) + 1.95 \, z. \quad (15)$$

This luminosity is the resulting characteristic brightness at $z = 0$ to which the galaxies would fade, assuming a pure passive evolution. The rate of luminosity evolution in equation 15 is consistent with the predictions of stellar population synthesis models that formed the bulk of the stars in E+S0 galaxies at $z \gtrsim 1.5$ (Bell et al. 2004).

In Figure 21 we compare the evolution of the rest-frame luminosity $M_B(z=0)$ (corrected for expected passive evolution) and stellar mass as a function of redshift for various field early-type galaxy samples. Several implications can be drawn from this diagram. First, there is a clear trend of $M_B(z=0)$ becoming more luminous with increasing redshift for the field E+S0 galaxies in the FDF and WHDF (large squares). Our results are in good agreement with the findings for field E+S0 galaxies up to $z \sim 1$ by Treu et al. (2005), shown as small triangles together with their associated errors (1σ scatter). These measurements have also been corrected with equation 15, but using the evolution as derived from their FP.

Moreover, the brightening detected for our galaxies indicates that the most massive E+S0 galaxies are the first to build up the red sequence whereas less massive ones join at more recent epochs ($z \lesssim 1$). The observed trend of both the evolutionary corrected luminosity and total stellar mass is consistent with that of a characteristic redshift evolution of the so-called "quenching" mass $M_Q \propto (1+z)^{4.5}$ (Bundy et al. 2006). The quenching mass limit $M_Q(z)$ is a diagnostic that traces the total baryonic (stellar) mass scale and a direct by product of the mechanism that drives downsizing. It is defined as the fraction of star forming galaxies (usually 1/3 of the total fraction) which contributes to the total (star forming) mass budget. Above this mass threshold $M_Q(z)$, star formation in stellar systems is suppressed and the majority of galaxies have already been transformed into passive, quiescent galaxies. The global trend of a downward evolution of the transitional mass with increasing age of the Universe, where $M_Q(z)$ decreases by a factor of ~ 5 from $z \sim 1$, is well reproduced by measurements based on the COMBO-17 and DEEP2 redshift surveys (Borch et al. 2006; Bundy et al. 2006; Hopkins et al. 2007). This transitional (crossover) mass is computed in different redshift bins for 50% late-type (spirals and peculiars) morphologies (dashed line in Figure 21), 50% galaxies with blue $(U - B)$ colour (dot-dashed line), and 50% galaxies with [O II] -inferred SFRs above 0.2 $M_\odot$ yr^{-1} (dotted line). These trends can also be fairly well described by the solid line in Figure 21,
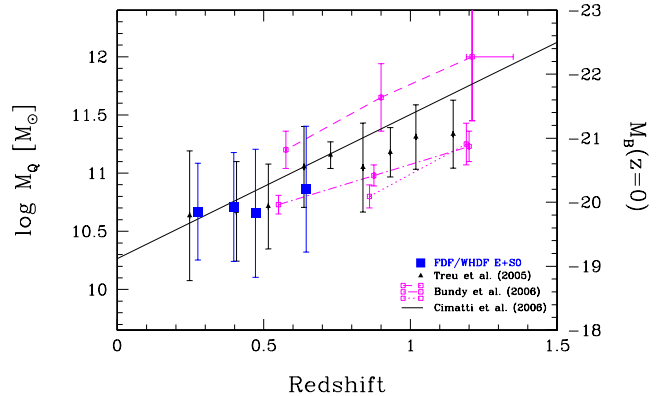

Figure 21. Evolution of the quenching mass M_Q and rest-frame luminosity (corrected for passive evolution) for different redshift bins. Field E+S0 galaxies in the FDF and WHDF are denoted by large squares, field E+S0s by Treu et al. (2005) as triangles. The evolution of the quenching mass by Bundy et al. (2006) is shown for three different sets of field galaxies, for 50% of late-type morphologies (dashed), 50% galaxies with blue $(U - B)$ colour (dot-dashed), and 50% with high [O II] SFR (dotted). The solid line indicates the passively evolved average LF for E+S0 galaxies by Cimatti et al. (2006) at which about 60% of the E+S0 galaxies are already in place. There is a weak decrease of $M_Q(z)$ towards lower redshifts, which suggests that star formation is efficiently suppressed in more massive galaxies.

which indicates the average evolution of the passively evolved LF for early-type galaxies from the COMBO-17, DEEP2 and SXDS with redshift (Cimatti et al. 2006) at which the bulk ($\approx 60\%$) of the E+S0 galaxies are already in place. While our observed field galaxies are in good agreement with the model predictions using blue $(U - B)$ color criterion, in particular for fainter (hence lower mass) individual field galaxies ($M_B(z = 0) > -20.5$, $M < 10^{11} M_\odot$), models with high SFR (as measured from the [O II] emission strength) are not consistent with the observations. There is a weak increase of the quenching mass $M_Q(z)$ with redshift which is already apparent at lower redshifts $z < 0.7$, which continuous up to higher redshifts $z \sim 1.2$. This trend suggests that star formation is more effectively suppressed in more luminous (massive) systems. Strong suppression of star formation could be triggered from AGN feedback of weak low luminosity (radio-mode) AGN that have red optical colours and are situated in very massive dark matter haloes (Croton et al. 2006; Salim et al. 2007).

Figure 21 suggests further that the evolution is a strong function of luminosity and mass and the evolution depends on the (evolution corrected) luminosity and stellar mass range of each specific galaxy sample under consideration. Evidence for this trend is also accumulated by studies of the redshift evolution of the LF, which argue that the number density of massive E+S0 galaxies ($M > 10^{11} M_\odot$) remains constant out to $z \sim 1$ (Bell et al. 2004; Cimatti et al. 2006). For less massive galaxies ($M < 10^{11} M_\odot$), the LF becomes progressively underpopulated with increasing redshift, which could point to the fact that the progenitors of the massive local E+S0 galaxies are still experiencing a period of active star formation. These galaxies would be too blue to fulfill the requirements in the LF selection at higher redshift, and could gradually build up the red sequence of massive E+S0 galaxies by a successive quenching of the star formation at the less massive end of the LF ($M < 10^{11} M_\odot$). In this picture, a fraction of blue (spiral) galaxies experience a rather slow, gradual morphological transformation into red, 'dead' quiescent E+S0 galaxies by a progressive quenching of star formation since redshifts $z \lesssim 1.2$.

8 CONCLUSIONS

Using a combination of high signal-to-noise intermediate-resolution VLT spectroscopy, deep $UBgRI$ ground–based photometry, and high-resolution ACS imaging, we have investigated the properties and evolution of 24 field early-type (E+S0) galaxies covering redshifts $0.20 < z < 0.75$ down to a magnitude limit of $M_B \leq -19.30$. The targets were selected from the southern FDF and northern WHDF based on morphology, luminosity, spectrophotometric type, and photometric redshift or broad-band colours. Scaling relationships of the Faber-Jackson relation (FJR), and Kormendy relation as well as the Fundamental Plane (FP) have been constructed to assess the evolution of the stellar populations for the galaxies in our sample. The formation epoch for the bulk of the stars in these systems was constrained by comparing the evolution of the M/L ratios to different stellar population models. To reveal the origin of the star formation in some of our galaxies, we have exploited the *Chandra* and *XMM-Newton* data archives. The main results of this work can be summarised as follows:

• The mass-to-light ratio of the field early-type galaxies evolves on average as $\Delta \ln(M/L_B) = -(1.71 \pm 0.18)\,z$, which is faster than for cluster early-type galaxies. This is consistent with field E+S0 galaxies comprising on average younger stellar populations than those of their cluster counterparts.

• The evolution as derived from the scaling relations of the FJR, the FP and hence the effective mass-to-light ratio shows a strong dependence on the mass. Less-massive systems with $M < 2 \times 10^{11} M_\odot$ display a faster M/L evolution of $\Delta \ln(M/L_B) = -(1.25 \pm 0.30)\,z$, whereas more-massive galaxies with $M > 2 \times 10^{11} M_\odot$ evolve much slower as $\Delta \ln(M/L_B) = -(0.89 \pm 0.19)\,z$. This implies that for the most massive field galaxies ($M > 2 \times 10^{11} M_\odot$) the majority of their stellar populations have been formed early at $z_{\rm form} = 3.5 \pm 1.3$. For less-massive galaxies the evolution in the M/L ratios can be translated into a lower formation redshift of their stars of $z_{\rm form} = 1.9 \pm 0.5$, which is at variance with the predictions of single-burst stellar population models. A fraction of 5%–10% in the total stellar mass of lower-mass galaxies ($M < 2 \times 10^{11} M_\odot$) must have been formed at more recent epochs. At $z = 0.4$, an accelerated evolution for less-massive galaxies ($\langle \Delta \ln(M/L_B) \rangle = -0.54 \pm 0.07$) than for more-massive ones ($\langle \Delta \ln(M/L_B) \rangle = -0.31 \pm 0.06$) is significant on the 2σ level.

• The morphological sub-classes of early-type galaxies, elliptical and lenticular (S0) galaxies, appear not to represent a homogenous group but follow different evolutionary tracks. Lenticular galaxies feature on average a stronger luminosity evolution ($\langle \Delta \ln(M/L_B)\rangle = -0.24 \pm 0.10$), bluer rest-frame colours and more diverse stellar populations and hence evolve faster than elliptical galaxies ($\langle \Delta \ln(M/L_B)\rangle = -0.09 \pm 0.07$). However, the differences between elliptical and lenticular galaxies are only moderate significant and difficult to disentangle from their individual scatter. Note that for deriving the scatter we took into account random errors as well as systematic uncertainties (see § 4.5). Interestingly, the scatter appears to be mainly amplified for lenticular galaxies.

• Evidence for secondary star formation activity in some of our galaxies is provided by the detection of [O II] emission or strong Hδ Balmer absorption as well as bluer rest-frame $(B - I)$ colour diagnostics. The Hδ absorption line strengths in our galaxies implies that the residual (low level) star formation of the galaxies accounts for 5% to 10% in the total stellar mass budget of these systems.

• We have found three possible candidates that could harbour an central AGN source. However, the trigger of the star formation in our galaxies is most likely either stellar origin or the result of AGN feedback from weak low luminosity (radio-mode) AGN with red optical colours (Croton et al. 2006; Salim et al. 2007).

• Over the past ∼6 Gyr, there is the trend of a slow decreasing quenching mass, which characterises a crossover in stellar mass above star formation in galaxies gets suppressed. This suggest that our systems experience a gradual suppression in their star formation processes. Our results favour a scenario where star formation is not immediately suppressed for less-massive halos and hence works on longer time scales in lower-mass galaxies.

The evolution of the M/L ratio of our field early-type galaxies favours a downsizing formation scenario, similar to the detected decrease in luminosity of rapidly star forming field galaxies since $z \sim 1$ (Cowie et al. 1996; Gavazzi et al. 1996). In this 'top-down' picture, massive galaxies are dominated by quiescent (red, old) stellar populations and evolve passively on longer timescales. Less-massive systems, however, exhibit more extended star formation histories with mass hosting star formation processes decreasing as times evolves. Both, the mass assembly and star formation are accelerated in massive stellar systems that are preferably located in high density environments. In contrast, in less-massive (smaller) systems, these physical processes work on longer timescales. Moreover, our results suggest a continuous mass assembly of field early-type galaxies during the last 5 Gyr. This is supported by recent studies of field galaxies up to $z \sim 1$ (van der Wel et al. 2005; Treu et al. 2005; Bundy et al. 2006; Hopkins et al. 2007).

An accelerated evolution in the M/L ratios of the less-massive galaxies with respect to more-massive ones was also found for *cluster* early-type galaxies (Fritz et al. 2005). The lack of a significant age difference between field and cluster early-type galaxies as expected from hierarchical formation models (Diaferio et al. 2001; De Lucia et al. 2004), and the dependence of the evolution on galaxy mass suggests that environmental effects play a rather minor role in the formation of early-type galaxies. More important to the evolutionary history of a stellar system are its internal properties, such as chemical composition or element abundance ratios.

In a next step, we will combine our precise FP measurements with an analysis of the absorption line strengths in our field early-type galaxies. This will provide strong constraints on the evolution of stellar populations and the chemical enrichment history of heavy elements in these systems.

REFERENCES

Appenzeller, I., Fricke, K. J., Fürtig, W., et al. 1998, The Messenger, 94, 1

Balogh, M. L., Morris, S. L., Yee, H. K. C., Carlberg, R. G., & Ellingson, E. 1997, ApJ, 488, L75

Baugh, C. M., Cole, S., Frenk, C. S., & Lacey, C. G. 1998, ApJ, 498, 504

Bell, E. F., & de Jong, R. S., 2001, ApJ, 550, 212

Bell, E., McIntosh, D. H., Katz, N., & Weinberg, M. D. 2003, ApJS, 149, 289

Bell, E. F. et al. 2004, ApJ, 608, 752

Bender, R., 1990, A&A, 229, 441

Bender, R., Saglia, R. P., Ziegler, B., Belloni, P., Bruzual, G., Greggio, L., & Hopp, U. 1998, ApJ, 493, 529

Bender, R., et al. 2001, in ESO Astrophysics Symp., Deep Fields, ed. S. Cristiani, A. Renzini, & R. E. Williams, Springer, p. 96

Benson, A. J., Ellis, R. S., & Menanteau, F. 2002, MNRAS, 336, 564

Bertin, E., & Arnouts, S. 1996, A&AS, 117, 393

Birnboim, Y., Dekel, A., & Neistein, E. 2007, MNRAS, 380, 339

Borch, A., et al. 2006, A&A, 453, 869

Bower, R. G., Benson, A. J., Malbon, R., Helly, J. C., Frenk, C. S., Baugh, C. M., Cole, S., Lacey, C. G. 2006, MNRAS, 370, 645

Böhm, A., Ziegler, B. L., Saglia, R. P., et al. 2004, A&A, 420, 97

Böhm, A., & Ziegler, B. L. 2007, ApJ, 668, 846

Bruzual, G. A., Charlot, S. 2003, MNRAS, 344, 1000

Bundy, K., et al. 2006, ApJ, 651, 120

Bundy, K., et al. 2008, ApJ, 681, 931

Chapman, S. C., Smail, I., Blain, A. W., & Ivinson, R. J. 2004, ApJ, 614, 671

Cimatti, A., Daddi, E., & Renzini, A. 2006, A&A, 453, L29

Cole, S., Lacey, C. G., Baugh, C. M., & Frenk, C. S. 2000, MNRAS, 319, 168

Conselice, C. J., et al. 2007, MNRAS, 381, 962

Cowie, L. L., Songaila, A., Hu, E. M, Cohen, J. G. 1996, AJ, 112, 839

Croton, D. J., et al. 2006, MNRAS, 365, 11

De Lucia, G., Kauffmann, G., & White, S. D. M., 2004, MNRAS, 349, 1101

De Lucia, G., Springel, V., White, S. D. M., Croton, D., & Kauffmann, G. 2006, MNRAS, 366, 499

Desroches, L.-B., Quataert, E., Ma, C.-P., & West, A. A. 2007, MNRAS, 377, 402

Diaferio, A., Kauffmann, G., Balogh, M. L., White, S. D. M., Schade, D., & Ellingson, E. 2001, MNRAS, 323, 999

di Serego Alighieri, S., et al. 2005, A&A, 442, 125

Djorgovski, S., & Davis, M. 1987, ApJ, 313, 59

Dressler, A. 1980, ApJ, 236, 351

Dressler, A., Lynden-Bell, D., Burstein, D., Davies, R. L., Faber, S. M., Terlevich, R., & Wegner, G. 1987, ApJ, 313, 42

Faber, S. M., & Jackson, R. E. 1976, ApJ, 204, 668

Faber, S. M., Wegner, G., Burstein, D., Davies, R. L., Dressler, A., Lynden-Bell, D., & Terlevich, R. J. 1989, ApJS, 69, 763

Faber, S. M., et al. 2007, ApJ, 665, 265

Fabbiano, G. 1989, ARA&A, 27, 87

Ferreras, I., et al. 2005, ApJ, 635, 243

Fritz, A., Ziegler, B. L., Bower, R. G., Smail, I., & Davies, R. L. 2005, MNRAS, 358, 233

Fritz, A. 2006, PhD thesis, University of Göttingen

Fritz, A., Ziegler, B. L., Böhm, A., Balogh, M. L., Bower, R. G., Smail, I., & Davies, R. L. 2006, in *The Fabulous Destiny of Galaxies: Bridging Past and Present*, eds. V. LeBrun, A. Mazure, S. Arnouts & D. Burgarella, Paris: Frontier Group, p. 525

Gavazzi, G., Pierini, D., Boselli, A. 1996, A&A, 312, 397

Gavazzi, G., Bonfanti, C., Sanvito, G., Boselli, A., Scodeggio, M. 2002, ApJ, 576, 135

Gebhardt, K., Faber, S. M., Koo, D. C., et al. 2003, ApJ, 597, 239

Glazebrook, K., et al. 2004, Nature, 430, 181

Granato, G. L., De Zotti, G., Silva, L., Bressan, A., & Danese, L. 2004, ApJ, 600, 580

Heidt, J., Appenzeller, I., Gabasch, A., et al. 2003, A&A, 398, 49

Hopkins, P. F., Bundy, K., Hernquist, L., & Ellis, R. S. 2007, ApJ, 659, 976

Horne, K. 1986, PASP, 98, 609

Jørgensen, I., Franx, M., & Kjærgaard, P. 1995, MNRAS, 276, 1341

Jørgensen, I., Franx, M., & Kjærgaard, P. 1996, MNRAS, 280, 167

Jørgensen, I., Chiboucas, K., Flint, K., Bergmann, M., Barr, J., & Davies, R. 2006, ApJ, 639L, 9

Kauffmann, G., 1996, MNRAS, 281, 487

Kauffmann, G., & Haehnelt, M., 2000, MNRAS, 311, 576

Kennicutt, R. C., Jr. 1992, ApJ, 388, 310

Kewley, L. J., Geller, M. J., & Jansen, R. A. 2004, AJ, 127, 2002

Kim, D.-W., & Fabbiano, G. 2003, ApJ, 586, 826

Kim, D.-W., & Fabbiano, G. 2004, ApJ, 611, 846

Kinney, A. L., et al. 1996, ApJ, 467, 38

Kriek, M., et al. 2006, ApJ, 649, L71

Le Borgne, D., et al. 2006, ApJ, 642, 48

McGrath, E. J., Stockton, A., Canalizo, G. 2007, ApJ, 669, 241

Metcalfe, N., Shanks, T., Campos, A., McCracken, H. J., & Fong, R. 2001, MNRAS, 323, 779

Monaco, P., Murante, G., Borgani, S., & Fontanot, F. 2006, ApJ, 652L, 89

Möller, C. S., Fritze-v.Alvensleben, U., Fricke, K. J., & Calzetti, D. 2001, Ap&SS, 276, 799

Noll, S., et al. 2004, A&A, 418, 885

O'Sullivan, E., Forbes, D. A., Ponman, T. J. 2001, MNRAS, 328, 461

O'Sullivan, E., Ponman, T. J., & Collins, R. S. 2003, MNRAS, 340, 1375

Pahre, M. A., 1999, ApJS, 124, 127

Peng, C. Y., Ho, L. C., Impey, C. D., & Rix, H.-W. 2002, AJ, 124, 266

Rusin, D. & Kochanek, C. S. 2005, ApJ, 623, 666

Saglia, R. P., Bender, R., & Dressler, A. 1993, A&A, 279, 75 (SBD93)

Saglia, R. P., et al. 1997, ApJS, 109, 79

Salim, S., et al. 2007, ApJS, 173, 267

Salpeter, E. E. 1955, ApJ, 121, 161

Sarazin, C. L., Irwin, J. A., & Bregman J. N. 2000, ApJ, 544, L101

Sargent, W. L. W., Schechter, P. L., Boksenberg, A., & Shortridge, K. 1977, ApJ, 212, 326

Sérsic, J. L. 1968, Atlas de Galaxias Australes (Córdoba, Argentina: Observatorio Astronomico, Univ. Nac. Córdoba)

Simard, L., et al. 2002, ApJS, 142, 1

Sirianni, M., Jee, M. J., Benítez, N., et al. 2005, PASP, 117, 1049

Somerville, R. S., & Primack, J. R. 1999, MNRAS, 310, 1087

Somerville, R. S., Primack, J. R., & Faber, S. M. 2001, MNRAS, 320, 504

Thomas, D., Maraston, C., Bender, R., de Oliveira, C. M. 2005, ApJ, 621, 673

Tinsley, B. M. 1980, Fundamentals of Cosmic Physics, 5, 287

Tonry, J., & Davis, M. 1979, AJ, 84, 1511

Treu, T., Stiavelli, M., Bertin, G., Casertano, S., & Møller, P. 2001 MNRAS, 326, 237

Treu, T., Stiavelli, M., Casertano, S., Møller, P., & Bertin, G. 2002, ApJ, 564, L13

Treu, T., et al. 2005, ApJ, 633, 174

van de Ven, G., van Dokkum, P. G., Franx, M. 2003, MNRAS, 344, 924

van der Wel, A., Franx, M., van Dokkum, P. G., Rix, H.-W., Illingworth, G. D., & Rosati, P. 2005, ApJ, 631, 145

van Dokkum, P. G., & Franx, M. 1996, MNRAS, 281, 985

van Dokkum, P. G., & Franx, M. 2001b, ApJ, 553, 90

van Dokkum, P. G., Franx, M., Kelson, D. D., & Illingworth, G. D., 2001a, ApJ, 553, L39

van Dokkum, P. G. & Ellis, R. S. 2003, ApJ, 592, L53

van Dokkum, P. G., & Stanford, S. A. 2003, ApJ, 585, 78

Weisskopf, M. C., Brinkman, B., Canizares, C., Garmire, G., Murray, S., Van Speybroeck, L. P. 2002, PASP, 114, 1

Woo, J. H, Urry, C. M., Lira, P., van der Marel, R. P., & Maza, J. 2004, ApJ, 617, 903

Woo, J. H, Urry, C. M., van der Marel, R. P., Lira, P., & Maza, J. 2005, ApJ, 631, 762

Worthey, G., & Ottaviani D. L. 1997, ApJS, 111, 377

Ziegler, B. L., Böhm, A., Fricke, K. J., et al. 2002, ApJ, 564, L69

Ziegler, B. L., Thomas, D., Böhm, A., Bender, R., Fritz, A., & Maraston, C. 2005, A&A, 433, 519

APPENDIX A: VERIFICATIONS OF σ MEASUREMENTS

A1 Different Absorption Passbands

To test the accuracy and the possible internal systematic effects of velocity dispersion measurements using different absorption features, galaxies where multiple σ determinations could be obtained are compared. In case of five field early-type galaxies in the WHDF σ was derived based on the Mg_b and the G-band feature. Figure A1 shows the formal relative uncertainty $\Delta\sigma/\sigma_1$ as a function of velocity dispersion (upper panel) and as a function of the S/N (lower panel) per Å for the early–type galaxies in the WHDF where both measurements are available. The lower panel is divided according to the S/N of the feature of interest, S/N values from the Mg_b lines are denoted as circles, whereas the S/N based on the G–band is indicated as triangles. $\Delta\sigma/\sigma_1$ was computed as the relative difference in velocity dispersion values of the Mg_b with the G-band line, normalised to the reference velocity dispersions σ_1. Both features were free from any contamination due to sky lines and did not suffer from any residual sky background artefacts. The relative uncertainties cover the range $0.03 \le \Delta\sigma/\sigma_1 \le 0.06$ with a median of $\langle\Delta\sigma/\sigma_1\rangle = 0.05$. The σ determinations are in extremely good agreement and show similar absolute errors between 8 to 18 km s^{-1}. Even for the lowest S/N ratios the formal uncertainty of 5% is less than the typical individual error in the σ measurement. This limit is also the smallest formal uncertainty that can be reached with the instrumental resolution and the template stars. No trend of increasing systematic errors on the σ values with low S/N can be found. Results from the Monte-Carlo simulations showed that the
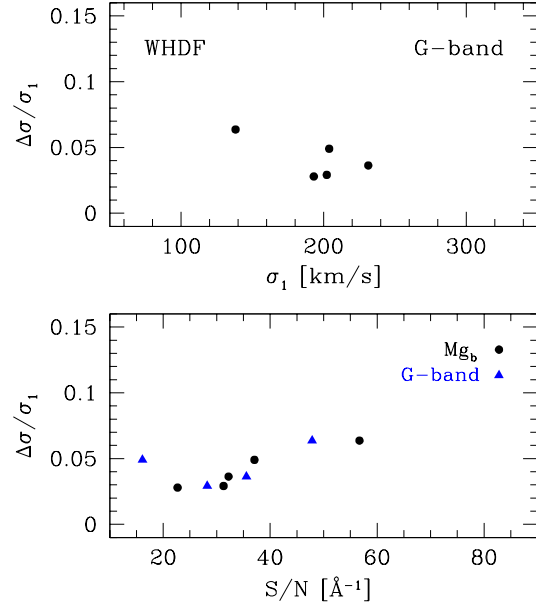

Figure A1. Comparison of velocity dispersion measurements derived from different absorption features. *Upper panel:* relative uncertainty of velocity dispersions with the G–band as a function of velocity dispersions σ_1 of early-type field galaxies in the WHDF. All galaxies are high quality σ measurements. *Lower panel:* $\Delta\sigma/\sigma_1$ versus the S/N per Å. Measurements are splitted according to the S/N of the feature (Mg_b circles, G–band triangles) to visualise possible systematic errors of low S/N on σ. For $S/N \ge 8$ Å^{-1}, effects of systematic uncertainties become negligible.

effects of systematic errors on σ become important at $S/N < 8$ per Å (cf. § 2.3.2). As this limit is below the average S/N in the spectra of our low–luminosity galaxies, the formal uncertainty therefore becomes negligible even for the lowest derived velocity dispersions in the galaxy samples. A comparison of the absolute velocity dispersions for the WHDF ellipticals is presented in Figure A2 in the next section.

A2 Repeat Observations

For a total of five field galaxies in the WHDF sample which are included in two or more different MOS masks, it is possible to confirm the internal reliability of the spectral reduction and analysis. A total of nine repeat observations was acquired for the WHDF ellipticals. Two galaxies were observed thrice (ID 92 and ID 111) and ID 173 four times. The velocity dispersions have been measured for both individual setups and the agreement between these two determinations is very good with a median offset in σ at the 4% level. Figure A2 compares the velocity dispersion measurements for the five WHDF field galaxy spectra which were observed with two or up to four different mask setups. One galaxy with four repeat observations is denoted with two additional large circles. In general, velocity dispersions of the secondary measurements are based on lower S/N spectra and therefore show larger errors. The final measurement with the smallest error yielded $\sigma_{173} = 204 \pm 16$ km s^{-1} ($S/N = 37$), which represents also the smaller deviation with respect to the reference line. For the WHDF field ellipticals the relative difference between reference and secondary measurements is $\delta\sigma/\sigma_1 = 0.041 \pm 0.015$ with $23 \le S/N \le 57$. In order to increase the signal–to–noise in the final spectra, these repeat obser-
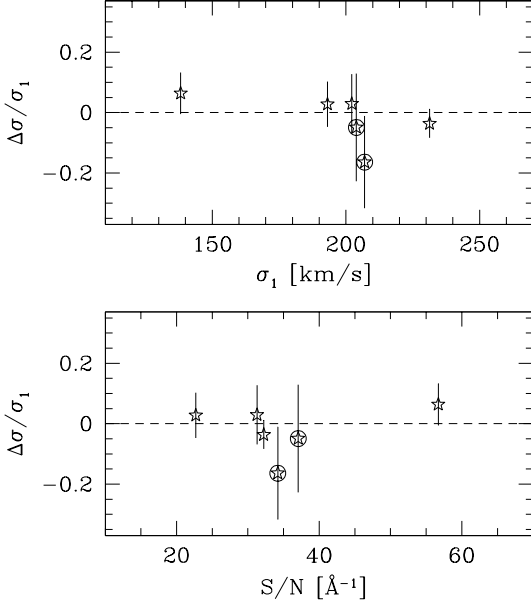
Figure A2. Comparison of velocity dispersion measurements for FORS2 spectra of field galaxies in the WHDF which have been observed with two different MOS mask setups and slitlet positions. One galaxy with four measurements is denoted with two additional large circles.

vations have been co–added. The repeated σ measurements in different slitlet configurations prove that our kinematic measurements are very stable and that internal effects such as varying spectral wavelength range and slitlet position on the FORS spectrograph can be neglected.

APPENDIX B: X-RAY POPULATIONS

Early-type galaxies in the nearby universe with luminosities typically $L_X \gtrsim 10^{42}\,\mathrm{ergs\,s^{-1}}$ most likely harbour an AGN source in their centre (O'Sullivan et al. 2001). Below this flux limit at $L_X < 10^{42}\,\mathrm{ergs\,s^{-1}}$, the main contributions to the total X-ray luminosity of a galaxy could be a variety of sources, such as from low-luminosity AGN (LLAGN), high-mass and low-mass X-ray (stellar) binaries (LMXBs) and emission fluxes from the diffuse soft X-ray plasma that surrounds the galaxy ($T_{\mathrm{eff}} < 1\,\mathrm{keV}$).

LMXBs are associated with evolved old stellar populations (A stars) and a common feature in local bulge systems in the field and globular clusters. As both E and S0 galaxies comprise homogenous stellar populations, their X-ray binaries (XRB) populations should also be uniformly distributed among the galaxy populations. In the past it was proposed that LMXBs might even dominate the global X-ray emission of early-type galaxies (Fabbiano 1989). However, this issue is hard to quantify as LMXBs cannot be identified as individual point sources. On the other hand for fainter X-ray systems observations argue that LMXBs account for a significant high fraction (from 20% up to 50%) of the X-ray emission of the host galaxy (Sarazin et al. 2000; Kim & Fabbiano 2003), which becomes a non-negligible factor when estimating the dynamical masses of their stellar host systems.

In oder to identify in our sample of galaxies with possible associated X-ray counterparts (see § 3.5) those systems with nuclear activity or ongoing star formation, an effective way would

be to classify our galaxies schematically based on their measured X-ray luminosity. Using the X-ray flux measurements for our objects, we can give constraints on the various sources that contribute to the X-ray emission of our galaxies. The two main groups of interests are systems with nuclear activity based on the X-ray luminosity (XAGN) and galaxies with low-luminosity nuclear activity (LLAGN) and/or ongoing star formation.

For the old quiescent stellar populations in early-type galaxies, pointlike X-ray sources are very likely to be entirely resembled by LMXBs. The contribution due to LMXBs is direct proportional to the stellar mass of a galaxy. In general, these binary systems ($\sim 30 - 140$ sources per galaxy) account for a smaller but non-negligible fraction ($\lesssim 25\%$) of the total galaxy X-ray luminosity (O'Sullivan et al. 2001; Kim & Fabbiano 2004). Using the relationship between total B-band and X-ray luminosity by Kim & Fabbiano (2004) as $L_X(\mathrm{LMXB}) = (0.90 \pm 0.50) \times 10^{30}\,L_B/L_{B,\odot}$ (in units of $\mathrm{ergs\,s^{-1}}$), we measure an average contribution of LMXBs of $\leq 17\% \pm 7\%$. The evolution corrected absolute B-band luminosities of our galaxies fall in the range $9.95 < \log(L_B/L_{B,\odot}) < 11.30$ with a median of 10.47. As a comparison, introducing our K-band measurements of $10.68 < \log(L_K/L_{K,\odot}) < 11.79$ (average 11.22) and a similar relation as above but for the K-band luminosity of $L_X(\mathrm{LMXB}) = (0.20 \pm 0.08) \times 10^{30}\,L_K/L_{K,\odot}$ ($\mathrm{ergs\,s^{-1}}$), we detect an LMXB source contribution of $\leq 18\% \pm 6\%$.

Local early-type galaxies show a correlation of their soft X-ray luminosity with their stellar L_B (e.g., O'Sullivan et al. 2001). Excluding dwarf galaxies, brightest cluster/group galaxies and galaxies with AGN hosts, O'Sullivan et al. (2001) found for 184 nearby E+S0 galaxies $\log(L_X) = (2.17 \pm 0.11)\log L_B + 17.98 \pm 1.12$. Because of the evolved stellar populations in the local E+S0 galaxies, any detected excess with respect to this empirical relation would imply a measure of star formation processes or LLAGNs in our distant galaxies. Applying the above relationship to our sample, we derive an excess in diffuse plasma fraction of $\leq 26\% \pm 15\%$ compared to the local value. Using instead the relation by O'Sullivan et al. (2003) $L_X(0.5 - 2.0\,\mathrm{keV}) = 4 \times 10^{41}\,(L_B/10^{11})^{2.7}$, the fraction of soft X-ray plasma decreases to $\leq 7\% \pm 3\%$. Both measurements give evidence for a weak excess in the X-ray luminosities in our distant galaxies ($10^{40} < L_X < 10^{42}$) compared to the local reference. The increased luminosities are most likely the result of a combination of star formation and/or LLAGN. However, a possible contribution from LMXBs and soft diffuse X-ray plasma emission to the X-ray luminosities cannot be ruled out completely. To clearly distinguish between the various contributions a detailed analysis of the X-ray spectra is necessary which goes beyond the scope of the present work.

This paper has been typeset from a TEX/ LATEX file prepared by the author.